# Eruption frequency and magnitude in a geothermally active continental rift

Tadesse, A. Z.; Fontijn, K.; Melaku, A. A.; Gebru, E. F.; Smith, V. C.; Tomlinson, E.; Barfod, D.; Gopon, P.; Bégué, F.; Caricchi, L.; Laha, P.; Terryn, H.; Gudbrandsson, S.; Yirgu, G.; Ayalew, D.

*Published in:*
Journal of Volcanology and Geothermal Research

*DOI:*
10.1016/j.jvolgeores.2022.107471

*Publication date:*
2022

# Eruption frequency and magnitude in a geothermally active continental rift: The Bora-Baricha-Tullu Moye volcanic complex, Main Ethiopian Rift

A.Z. Tadesse[1*], K. Fontijn[1,2], A.A. Melaku[3], E.F. Gebru[3,4], V.C. Smith[5], E. Tomlinson[6], D. Barfod[7], P. Gopon[2,8], F. Bégué[9], L. Caricchi[9], P. Laha[10], H. Terryn[10], S. Gudbrandsson[11], G. Yirgu[3], D. Ayalew[3]

[1]Department of Geosciences, Environment and Society, Université libre de Bruxelles (ULB), Belgium.

[2]Department of Earth Sciences, University of Oxford, UK.

[3]School of Earth Sciences, Addis Ababa University (AAU), Ethiopia.

[4]Department of Geosciences, Université de Fribourg (UNIFR), Switzerland.

[5]Research Laboratory for Archaeology and the History of Art, University of Oxford, UK.

[6]Department of Geology, Trinity College Dublin (TCD), Ireland.

[7]NEIF Argon Isotopes, Scottish Universities Environmental Research Centre, UK.

[8]Department of Applied Geosciences and Geophysics, University of Leoben, Austria.

[9]Department of Earth Sciences, University of Geneva (UNIGE), Switzerland.

[10]Research Group of Electrochemical and Surface Engineering, Department of Materials and Chemistry, Vrije Universiteit Brussel (VUB), Belgium.

[11]Reykjavik Geothermal Ltd, Iceland.

*Corresponding author: Amdemichael.Tadesse@ulb.be, amdemichaelz@gmail.com, Tel +32471309363

**Abstract**

Many Quaternary silicic volcanoes in the Main Ethiopian Rift pose a potential risk due to the poorly known eruptive histories of the volcanoes in combination with a high population density. In this study we provide new constraints on the Late Pleistocene-Holocene eruptive history of the Bora-Baricha-Tullu Moye (BBTM) volcanic complex located in the central portion of the Main Ethiopian Rift (MER). BBTM constitutes three main silicic edifices (i.e. Bora, Baricha and Tullu Moye) and numerous smaller vents (including Oda and Werdi). Tephra deposits from these vents are several centimetres to meters in thickness in currently densely populated regions and where geothermal development is taking place. We present new field observations in addition to physical, petrographic, geochemical and geochronological data. BBTM experienced at least 27 explosive eruptions, of varying magnitude, in the last ca. 100 ky. The two oldest tephra deposits in our compiled stratigraphy are associated with large-magnitude, and possibly caldera-forming eruptions. The youngest of these (Meki) occurred at 107.7 ± 8.8 (2σ) ka, which makes it the youngest caldera-forming eruption identified in the Central MER so far. During the post-caldera stage, BBTM underwent at least 25 eruptions sourced from the Baricha (9 eruptions), Bora (3), Oda (8), Werdi (3) and Tullu Moye (2) edifices. The return period of explosive activity in BBTM is thus at least one moderate-to-large explosive eruption every 4000 yr. Well-exposed units have estimated eruption magnitudes (M) that are 4 to 5, while smaller-scale eruptions reach up to 2.5 and are exclusively preserved near the Tullu Moye vent. The tephra was dispersed up to 20 km from the volcanic complex suggesting that more than one hundred thousand

people could be exposed to tephra fall and pyroclastic density current hazards from future of similar-magnitude eruptions in this area.

**Key words**

Bora-Baricha-Tullu Moye; Main Ethiopian Rift; tephrostratigraphy; explosive eruptions

## 1. Introduction

The Main Ethiopian Rift (MER) is a mature volcano-tectonic rift zone with Quaternary silicic volcanoes arranged regularly along the rift axis, and numerous small, fault-controlled mafic eruptive centres (Fig. 1). The silicic volcanoes have produced hundreds of cubic kilometres of highly evolved magmas, and many of them host large caldera depressions and geologically young (i.e. Late Pleistocene-Holocene) edifices formed in the post-caldera stage (e.g. Corbetti: Rapprich et al. 2016; Aluto: Hutchison et al. 2016a, b; and Gedemsa: Peccerillo et al. 2003; Fig. 1). Many of these volcanoes pose a high-risk due to the high population density and their poorly known eruptive histories (Aspinall et al. 2011; Loughlin et al. 2015). Long repose periods (several 100 to 1000 years for some MER volcanoes; Martin-Jones et al. 2017; Fontijn et al. 2018; McNamara et al. 2018; Siegburg et al. 2018) further compromise hazard awareness and, thus, efforts to reduce or mitigate the risk (e.g. Donovan & Oppenheimer 2012). Several MER volcanoes currently show signs of geophysical unrest, primarily in the form of ground deformation detected by satellite radar interferometry (Biggs et al. 2011; Hutchison et al. 2016c; Albino & Biggs 2021). The current study focuses on one of these volcanoes (Bora-Baricha-Tullu Moye) with the aim to improve

66 our understanding of its eruptive history and the related hazard for neighbouring
67 populations and socio-economic development.

68 The Bora-Baricha-Tullu Moye (BBTM) volcanic complex is located in the central portion of
69 the MER (Fig. 1). Bora, Baricha and Tullu Moye are the three main silicic edifices, among
70 several smaller ones (including Oda and Werdi, Fig. 2). At present BBTM is active and has
71 experienced ongoing low frequency seismicity (e.g. Greenfield et al. 2019 a, b) and episodic
72 ground deformation over at least the past decade (Biggs et al. 2011; Albino & Biggs 2021).

73 The earliest reconnaissance studies on the distribution of the volcanic products were
74 performed in the 1970s (Di Paola 1972; Bizouard & Di Paola 1978) and recognised that Tullu
75 Moye (in the east of the complex) mainly erupts comendites, and pantellerites are mainly
76 found in the west, around Bora and Baricha. Since then, several studies have focused on the
77 geothermal potential of the area that is 500 MWe annually (UNDP 1973; ELC 1987; Mamo
78 2002; Varet & Birba 2018). At the time of writing, the area is at an advanced geothermal
79 exploration stage, with ongoing drilling operations that are mainly located on the eastern
80 side (Tullu Moye) of the complex. The location of this significant investment project and the
81 high population density of the area located in towns such as Meki, Alem Tena, Iteya and
82 Assela, all within 20 km of at least one of the main volcanic edifices, motivated this
83 volcanological study.

84 BBTM experienced several explosive eruptions in the past as identified from a preliminary
85 stratigraphic sequence presented by Fontijn et al. (2018). This study builds on their previous
86 work, providing new field observations, physical (componentry), petrographic, geochemical
87 (glass major and trace element geochemistry), and geochronological ($^{40}Ar/^{39}Ar$ and $^{14}C$) data
88 on pyroclastic deposits across the BBTM. We establish a tephrostratigraphic framework for

89 the BBTM volcanic field to constrain the frequency-magnitude relationship of the eruptive
90 events at this active caldera system.

91

92 **2. Geological Setting**

93 The MER is an active rift zone stretching between the Afar and Turkana depressions in the
94 East African Rift (EAR). The MER is bounded by roughly NE-SW oriented border faults
95 separating the surrounding Eastern and Western Plateaux. The rift gradually narrows from
96 the southern Afar depression into the MER with a minimum width of ~80 km. The southern
97 MER boundary is considered to be located at ~5°N latitude (Balestrieri et al. 2016) where a
98 ~300 km-wide system of basins and ranges called the Broadly Rifted Zone exists (Ebinger et
99 al. 2000). Here, the rift zone widens and the deformation becomes more distributed.

100 The present-day configuration of the MER suggests the progressive narrowing of volcano-
101 tectonic activity with time that will eventually lead to continental breakup and subsequent
102 oceanic spreading (e.g. Ebinger & Casey 2001; Ebinger 2005; Rooney et al. 2007; Daly et al.
103 2008; Bastow et al. 2011). The Quaternary deformation and volcanism have mainly
104 concentrated on the axial magmatic segments that are located along a 20 x 60 km zone (i.e.
105 Wonji Fault Belt, WFB; Ebinger & Casey 2001; Keir et al. 2006). In these magmatic segments
106 the younger products erupted from volcanic fissures, scoria cones and large central
107 volcanoes are collectively known as the Wonji group (e.g. WoldeGabriel et al. 1990). This
108 group is dominated by silicic volcanic rocks erupted from the large central volcanoes aligned
109 along the axial zone of the MER (i.e. Corbetti, Aluto, BBTM, Gedemsa, Boku, Boset-Bericha,
110 Kone and Fentale; Fig. 1). These volcanoes are systematically spaced (ca. 20-45 km apart),
111 with edifices rising hundreds of meters above the MER plain. Some of these large silicic

112 edifices are associated with well-developed caldera structures (e.g. Kone, Gedemsa), where
113 others have calderas that are largely concealed by post-caldera eruptive products (e.g.
114 Aluto). The post-caldera eruptive products primarily occur as silicic tephra deposits and
115 (obsidian) lava flows (e.g. Peccerillo et al. 2003; Hutchison et al. 2016a, b; Rapprich et al.
116 2016; Fontijn et al. 2018).

117 Volcanic products from the present-day BBTM volcanic centres, including Bora, Baricha and
118 Tullu Moye, overlie Late Pleistocene ignimbrites that have been K-Ar dated to 1.58 ± 0.2 Ma
119 (Table 1; WoldeGabriel et al. 1990). Three borehole wells (TG-1, TG-2 and TG-3; Fig 2) show
120 that the BBTM subsurface geology consists of trachyte and rhyolite lava flows at the base,
121 which are overlain by weakly to moderately compacted layers of ignimbrites and unwelded
122 pyroclastics (Ayele et al. 2002). The rhyolite lavas thin out and the fine-grained ignimbrites
123 become very thick (87.5 m) at TG-2. Another well (TG-4) drilled near a rhyolite dome
124 (Adano) shows very thick (100 m) trachytic and rhyolitic lavas with variable porphyritic to
125 fully glassy (obsidian) texture overlaying an ignimbrite similar to that observed in the rift
126 escarpment (Ayele et al. 2002). Well TG-5 is located close to Tullu Moye volcano and
127 incorporates very thick (90.5 m) porphyritic and scoriaceous basalt at the base. The
128 subsurface lithologies show alteration that is likely related to the persistent hydrothermal
129 activity in the region (Ayele et al. 2002).

130 The surface geology of Bora and Baricha is characterized by poorly to completely unwelded
131 pumice and ash deposits (Di Paola 1972). Subordinate rhyolitic lavas are associated with the
132 pyroclastics at Baricha (e.g. Di Paola 1972; ELC 1987; Ayele et al. 2002). Near Baricha, Fontijn
133 et al. (2018) identified >7 pantelleritic pumice fall deposits alternating with poorly-

developed palaeosols. Several smaller pumice vents are located to the east of Bora and Baricha, including Werdi and Oda (Fig. 2).

Tullu Moye is situated in the intensely faulted part of the region (also known as the Salen range; Varet & Briba 2018) along the WFB, and has trachytic lavas and hydrothermally altered pyroclastic deposits. The whole rock (Bizouard & Di Paola 1978) and glass (Fontijn et al. 2018) chemical compositions indicate that Tullu Moye pumice and obsidian lava have a comenditic composition. The plain located to the NE and SW of Tullu Moye is covered by thick obsidian (at Giano and Janno/Miesa; Ayele et al. 2002) and basaltic flows and associated scoria, spatter and cinder cones. Those products erupted along fissures and conceal some of the earlier Tullu Moye tephra deposits (UNDP 1973; ELC 1987). The Giano obsidian flow (after Bizouard & Di Paola 1978) possibly erupted during historical time (ca. 1900 CE) and covers a 2.7 X 1.6 km area; though detailed accounts of the eruption or its exact age are not known (Gouin 1979).

Since the Late Cenozoic, tectonic activity in the MER caused subsidence and formed an asymmetric basin with fluvio-lacustrine sedimentation (e.g. Le Turdu et al. 1999). Today several lakes exist in this asymmetric MER floor (Fig. 1). Most of these lakes were repeatedly connected and disconnected in the Quaternary as a result of tectonic subsidence and/or lake level fluctuations (Benvenuti et al. 2002, 2013). At least two major lake expansion phases are recorded in the sediments (Benvenuti et al. 2002). The oldest “Megalake” phase occurred around the Late Pleistocene (ca. 100 ka) and is separated from a second lake level high-stand (“macrolake” phase, ca. 10 ka) by an erosional contact that resulted from prolonged low-stand and lake level fluctuations (e.g. Benvenuti et al., 2002; Le Turdu et al. 1999). The fluvio-lacustrine sediments are interbedded with volcanic (pyroclastic and

157 epiclastic) deposits, providing evidence for episodic volcanic activity throughout the Late
158 Quaternary (Le Turdu et al. 1999; McNamara et al. 2018). In the northern and central
159 portions of the MER these lacustrine sediments reach up to tens of meters of thickness (Le
160 Turdu et al. 1999; Benvenuti et al. 2002). Subsurface geophysical investigations (e.g.
161 Mulugeta et al. 2021) and deep boreholes (e.g. Teklemariam et al. 1996) around Aluto
162 volcanic complex reveal lacustrine deposits that are up to 600 m in thickness.

163

164 **3. Methods**

165 Field campaigns were performed in 2015, 2017 and 2020. A total of 162 outcrops were
166 systematically logged, and samples were collected for each stratigraphic unit from multiple
167 sites around the volcanic complex (Fig. 2a). Pyroclastic units were correlated using a
168 combination of field observations (including lateral tracing between outcrops), physical
169 characteristics and chemical compositions.

170 Componentry analysis was performed to quantify the proportions of different particle types
171 that occur in tephra deposits sourced from different centres across the BBTM. Eighty-five
172 samples, each up to 2 kg, from selected tephra layers, and in some cases from different
173 stratigraphic levels of the same deposit (e.g. base, middle and top) were dry-sieved at 1ϕ
174 intervals between -2ϕ (4 mm) and 2ϕ (0.25 mm). In each grain size fraction particles were
175 qualitatively assigned into classes, counted and weighed. The assigned classes are: (1)
176 Vesicular juvenile, which are unaltered to slightly altered pumiceous clasts; (2) Dense
177 juvenile, which are poorly- to- non-vesiculated, dense and fresh volcanic glass shards; (3)
178 Accidental dense lithics; and (4) Free crystals, which may be juvenile or xenocrystic. Each
179 class was described qualitatively according to colour, vesicularity, vesicle size, vesicle shape,

crystallinity and type (Houghton & Wilson 1989; Cas et al. 2008). Vesicular juvenile clasts of each bed-set were qualitatively described and classified based on colour (i.e. yellow-brown, dark-grey, light grey, bluish-grey and white) and clast textures using nomenclature as per Polacci et al. (2003): expanded (extensive vesicle expansion with >90% interconnected vesicles), microvesicular (equidimensional clasts containing heterogeneous vesicles) and tube (fairly elongated to highly stretched vesicles). The lithic fragments were qualitatively described according to their levels of alteration (i.e. reddish to light brown colour) and nature (lava, obsidian and green ignimbrite). The data presented in section 4.1 is the average of all analysed grain size fractions between 4 mm and 0.25 mm (see Table 2).

Thin sections of selected pyroclastic and lava samples were prepared by TS Lab and Geoservices, Italy. Modal mineral percentages were estimated by an automated point counting method using ImageJ (Schneider et al. 2012) and the image analysis toolbox Jmicrovision 1.3.1 (Roduit 2019). At least 300 points were counted per field-of-view. To measure the areas of vesicles and solid material (groundmass (typically glassy) and crystals), each phase was segmented by manual bi-level greyscale thresholding based on the histogram of the image. Vesicle and groundmass / crystal proportions were then recalculated using the mineral area proportions in the solid phase as obtained from the point counting.

For glass chemical analysis pumice lapilli were manually crushed using an agate pestle and mortar. The crushed samples were wet-sieved at 80 µm to remove the finer clay-sized fraction that cannot be analysed and dried in an oven at 50 $^{\circ}$C. The recovered fresh shards were cold-mounted in pre-drilled EpoFix resin discs and polished with SiC paper (grade P1200 and P2400) and diamond paste (3 and 1 micron). Back-scattered electron (BSE)

imaging and semi-quantitative compositional analyses were performed with a JEOL JSM-IT300 scanning electron microscope fitted with an Oxford instruments SDD X-MaxN EDS detector at the Department of Materials and Chemistry, Vrije Universiteit Brussel (VUB) to determine suitable points for qualitative glass analysis, avoiding phenocrysts and microlites. The SEM and EDS data for selected samples is displayed in the supplementary material (SM-1).

Glass major element data was acquired by Electron Microprobe Analysis (EPMA) using a JEOL JXA-8600 Superprobe (Research Laboratory for Archaeology and the History of Art, University of Oxford), a JEOL 8200 (Department of Earth Sciences, University of Geneva) and a CAMECA SX5-FE (Department of Earth Sciences, University of Oxford). On all three instruments, the same analytical protocol was used. Analyses were conducted on carbon-coated polished grain mounts using an accelerating voltage of 15 kV, a low beam current (6 nA) and a defocused beam of 10 µm. For samples with smaller glass areas, a 4 nA beam current and a probe diameter of 6 µm were used. Counting times on the peak were set to 30 seconds (Si, Al, Ti, Ca) and 60 seconds (P, Mg, Mn, Fe). Due to Na and K mobility and loss issues, Na and K were analysed first on each spectrometer, and were measured with a short peak count time of 12 seconds. The background count times at the high and low background where half of the peak count time. The instruments were calibrated with a suite of appropriate mineral standards, listed on supplementary material (SM-2). Analysis of secondary glass standards (ATHO-G, StHs6/80-G and MLB-3-G; Jochum et al. 2006) was used to regularly verify the calibration. The secondary standards analytical precision is typically < ± 4% relative standard deviation (RSD) for most major elements, except for the low abundance elements such as Ti (± 8%), Mn (± 30%) and P (± 38%). At least 20 individual points were analysed per sample. Only analyses with totals above 92 wt% were considered

reliable, and data were normalized to 100% before being plotted (Frogatt 1983; Lowe 2011). A representative set of analyses are presented in Table 3; the full data set is available in supplementary material (SM-2).

Trace element analyses of glass shards for some tephra units were conducted by Laser Ablation – Inductively Coupled Plasma – Mass Spectrometry (LA-ICP-MS) at the iCRAG laboratory, Trinity College Dublin (TCD) using a Teledyne Photon Machine G2 193 nm excimer laser ablation system with a two-volume Helex cell coupled to a Thermo Scientific iCAPQ ICP-MS. We used a spot size of 30 µm, a repetition rate of 5 Hz with a 35 s acquisition time with 30 s for washout between samples. Concentrations were calibrated using a NIST612 glass standard (using the composition reported by Jochum et al. 2011) with $^{29}$Si as the internal standard. During the measurement, the calibration was verified using MPI-DING glasses (ATHO-G and StHs6/80-G; Jochum et al. 2006). Data reduction was undertaken using Iolite 3.4. The secondary standards trace element analysis precision is typically ≤11% except for Rb, Sr, Y and Nb (≤7%) in RSD.

Two pumice samples (MER149A and MER147-2D) were prepared at the Department of Earth Sciences, University of Oxford for single-crystal $^{40}$Ar/$^{39}$Ar dating. The samples were crushed and sieved, and 250-500 µm size fractions were recovered. These fractions were cleaned in distilled water in an ultrasonic bath, dried in an oven at 50 °C and passed multiple times through a Frantz Isodynamic magnetic separator to concentrate sanidine crystals. The sanidine concentrates were leached in 5% HF to remove any adhering glass, and examined under a binocular microscope to collect pristine, inclusion-free, grains. Dating was performed at the NEIF Argon Isotope Laboratory at the Scottish Universities Environment Research Centre (SUERC), University of Glasgow. Samples and neutron flux monitors were

packaged in aluminium discs and stacked in quartz tubes for later reconstruction of neutron flux gradients. The sample package was irradiated in the Oregon State University reactor, Cd-shielded facility. Alder Creek sanidine (1.1891 ± 0.0008 (1σ) Ma; Niespolo et al. 2017) was used to monitor $^{39}Ar$ production and establish neutron flux values (J) for samples. Ar isotopic measurement was performed on a MAP-215-50 instrument, single-collector mass spectrometer using an electron multiplier collector. Blanks were analysed at the start and in between every run. Mass discrimination during the sample run was monitored and calibrated by analysis of air standards. Mass discrimination, nucleogenic interference and atmospheric contamination were corrected using MassSpec software (version 8.058). Ages were calculated using the decay constant factors after Renne et al. (2011) and yields an age of 107.7 ± 8.8 ka (MER149A) and 87 ± 16 ka (MER147-2D) with 2σ uncertainty.

One sample of charcoal embedded within a BBTM tephra deposit was sampled for accelerator mass spectrometry radiocarbon dating. The conventional age of 871 ± 24 $^{14}C$ yr BP was calibrated using Oxcal 4.4 (Bronk Ramsey 2009) using the IntCal20 calibration curve (Reimer et al. 2020). The calibrated radiocarbon age gives an age of 1190 ± 36 cal yrs BP (760 ± 36 CE) with a 95.4% probability interval.

After constraining the tephrostratigraphy, the tephra fall volume of individual deposits was estimated for some major eruptions by manually constructing isopachs, based on 4 to 10 data points. We calculated the minimum bulk deposit volumes using the Pyle (1989) and Legros (2000) method.

## 4. Results

### 4.1. Field stratigraphy and Geochronology

We identify 27 individual volcanic deposits that are all interpreted to be the products of separate explosive eruptions. The deposits are distinguished based on lithological (e.g. componentry, clast textures, glass geochemistry) and depositional characteristics. Most units are correlated at a local/sub-regional scale based on field and laboratory data, except for some of them (at least seven; section 4.1.8). In the following descriptions, the deposits are categorized on their interpreted source vent/area and described from the oldest to youngest for each category. Based on the distance from the vent area, the outcrops are defined as very proximal (<5 km from the vent), proximal (5-10 km), medial (10-30 km) and distal (>30 km). The identified stratigraphic units are labelled in systematic stratigraphic order from base to top, starting with two letters that represent the source vent (e.g. the basal pumice unit from Baricha is Ba-P1 and is overlain by Ba-P2). The location of each section is presented on Figure 2 and in supplementary material (SM-3). The overview of the stratigraphic record and unit correlations is shown on Figure 3. Key images and description of representative outcrops (Fig. 4; SM-3), componentry, and petrography (Fig. 5; SM-4) are also displayed on separate figures and all the data is included in the supplementary material. Table 2 represents the main characteristics of all BBTM deposits; descriptions of widely dispersed eruptive units (i.e. major deposits, correlated across at least 5 sections) are given below. In these descriptions, we simply mention the chemical composition of the units to support the correlations, but more details of the geochemistry are given in Section 4.2.

#### *4.1.1. Suke Deposit*

The Suke deposit is the oldest pyroclastic BBTM unit identified in the region. The base of the deposit is not observed, but the unit is overlain by a succession of Meki pumice (section

296 4.1.2) and porphyritic basaltic lava in different sites. Glass compositions of the Suke unit are
297 pantelleritic. The deposit is exposed at only a few locations (MER253 and MER367) in the
298 area of Suke, along a deep gully in the north-central part of the complex (Fig. 2). It has a
299 maximum thickness of 6 m at Suke (MER253) and is very poorly sorted, clast-supported, and
300 fine depleted, with bombs and lithic blocks up to 1 m in diameter of aphyric obsidian, dense
301 pumice and altered lava (Fig. 3a; Fig. 4). About 3 km east of the type locality, in section
302 MER367, the fine-grained component (<2 mm) with both pumiceous and lithic material
303 becomes dominant (>50%). The pumice is light to dark grey and very crystal poor with only
304 <1% of aenigmatite and no other visible crystals. The depositional characteristics indicate
305 that the Suke deposit is an ignimbrite with a lithic lag breccia facies in proximal section
306 MER253, and representative of pyroclastic density currents (PDCs) formed during a caldera-
307 forming eruption. The absence of any datable material (e.g. sanidine phenocrysts) prevents
308 us from constraining the absolute age of the Suke ignimbrite.

309

310 ***4.1.2. Meki Deposit (107.7 ± 8.8 ka)***

311 The Meki deposit is exposed in four places around the town of Meki (Fig. 2). It is also
312 underlain by the Suke deposit and overlain by tephra deposits sourced from Baricha (cf.
313 Section 5.1.3) in the Suke locality (MER253; Fig. 3a). At this latter location, the Meki deposit
314 is separated from both under- and overlaying units by weakly developed palaeosols. The
315 largest outcrop exposes >20 m of pyroclastic deposits in a quarry site near the Ziway-Meki
316 road (MER149 and MER326). There, the basal portion (up to 3 m exposed) of the sequence
317 is a well-sorted, massive, fine to coarse pumice lapilli breccia that is free of accidental lithics.
318 In this lower part of the quarry, at ca. 1660 m asl, distinct sub-horizontal brown staining on

319 the pumice surface is observed over a thickness of ca. 1 m in the MER149 and MER326
320 outcrops. The middle portion of the deposit is characterised by alternations of well-sorted
321 and poorly sorted fine lapilli breccia units that range between 10 and 90 cm in thickness.
322 The poorly sorted part of the deposit does not maintain a consistent local thickness and
323 becomes very thick (~13 m) in a section west of Meki town (MER327; Fig. 2a). At this section
324 the deposit is poorly sorted, displaying a variety of lenticular and wavy bedding, horizontal
325 laminations (alternation of mm-scale fine ash and lapilli layers), and in places mm-scale sub-
326 parallel to low-angle cross-bedding, with sub-rounded pumice lapilli in a fine ash matrix. The
327 upper ~8 m of the Meki deposit is, again, a massive, well-sorted and lithic-free pumice lapilli
328 breccia with ca. 10% of expanded pumice clasts. The deposit from the Meki section (i.e.
329 MER149) is virtually free of lithics and contains 80-95% pumice clasts (45-90%
330 microvesicular-light grey and ≤40% expanded-dark grey coloured pumice) and 5-20% free
331 crystals (alkali feldspar and aenigmatite) in the finer fractions below 1 mm. The pumice
332 clasts are highly vesicular (ca. 70-75% vesicularity), almost aphyric with ca. 1% phenocrysts
333 of alkali feldspar and aenigmatite, within a microlite-free groundmass. The Meki deposit has
334 distinct pantellerite glass compositions (section 4.2) relative to the Suke deposit, allowing
335 the correlation between the two main sequences in the area of Meki (west of the BBTM
336 complex) and Suke (central part; Fig. 2). At the Suke section, the Meki deposit is represented
337 by three stratigraphic horizons that show coarse lapilli at the base and matrix-dominated
338 massive beds at the top. The lack of an erosive surface or palaeosol between these horizons
339 suggests there was not a significant time gap between their depositions. Both in Suke and
340 Meki, we interpret the lower and upper portions of the deposit as a tephra fall, and the
341 middle part as a diluted PDC that is also interbedded with minor tephra falls. Sanidine

crystals from the lower part of the deposit were dated by $^{40}Ar/^{39}Ar$ to 107.7 ± 8.8 ka (Table 1).

### *4.1.3. Baricha Sequence*

The Baricha pyroclastic deposits are relatively widely dispersed to the West and well preserved in different stratigraphic sections. Some major units (i.e. well dispersed; Ba-P3 to Ba-P7) are observed in up to 25 different outcrops that extend 20 km from the summit of Baricha. The Baricha tephra sequence is stratigraphically younger than the Meki deposit, and the deposits commonly have lithics and a small proportion of expanded pumice lapilli. A deep gully (MER147) near Baricha exposes >9 distinct pantelleritic stratigraphic units (Fig. 3a). These units are separated by well-developed, 5 to >20 cm thick palaeosols. Other sections (e.g. MER205, MER301-3 and MER324) expose 6-8 individual deposits that can be correlated with the Baricha type section (MER147). Altogether, there are 5 major and 4 minor eruption deposits attributed to Baricha and sorted from oldest (Ba-P1) to youngest (Ba-P9) in Table 2. The major units are described in further detail here.

Ba-P3 is the oldest major Baricha deposit identified in a few proximal sections. A maximum thickness of ca. 3 m is observed in a section (MER205) located 4.5 km west from the summit. The basal 5-10 cm of the unit is composed of poorly sorted, well-indurated fine ash and accretionary lapilli. Above the bottom ash horizon, the deposit appears as a light grey coloured pumice lapilli breccia, that is well sorted and with massive to cm-scale crude bedding. The upper portion contains occasional pumice bombs (~15 cm) embedded in a sandy to silty cream-coloured horizon that is much more matrix-rich than the lower half of the deposit. The componentry of the middle portion of Ba-P3 shows 80-90% pumice clasts

(microvesicular), ≤20% free crystals in the finer fractions (feldspar, aenigmatite and orthopyroxene) below 1 mm and <1% lithics (crystal-rich obsidian). The pumice clasts are highly vesicular (ca. 65% vesicularity), moderately phyric with ca. 6% phenocrysts of alkali feldspar, aenigmatite and orthopyroxene in a glassy groundmass. We interpret the ash unit with accretionary lapilli and middle section of Ba-P3 formed by tephra fall and the upper portion, more matrix-rich, as the result of pedogenesis.

Above Ba-P3, a tripartite Baricha unit (Ba-P4) is exposed in different outcrops with a maximum total thickness of 3 m. The lower meter of the deposit comprises cm-scale alternations of fine lapilli and a yellowish ash bed. The rest of the deposit is massive and contains occasional pumice bombs of ~20 cm diameter in very proximal outcrops. The massive portion of the unit overlies a subtly normally graded 30 cm thick subunit; and it is composed of a clast-supported, poorly sorted, very coarse lapilli breccia. The componentry of the massive portion shows 45-80% pumice clasts (45-75% microvesicular, <5% expanded and ≤1% tube pumice), 10-35% free crystals (feldspar, aenigmatite, amphibole and Fe-Ti oxides) in the finer fractions and ≤10% lithics (crystal-rich obsidian, altered lava and ignimbrite). The pumice clasts are moderately vesicular (65% vesicularity), and almost aphyric, with <1% phenocrysts of alkali feldspar and aenigmatite, in a microlite-poor groundmass. The depositional characteristics indicate that the Ba-P4 deposit is a fallout tephra.

Ba-P5 is a widespread deposit identified to the West of Baricha. It is preserved in both proximal and medial outcrops, with a maximum thickness of 2.7 m. The unit is typically lithic-rich at the base and shows a gradual decrease in lithic proportion and other facies variations upwards in the stratigraphy. The bottom and top-third portions of the unit are

388 massive while the middle part shows cm-to-dm-scale diffuse bedding of generally well
389 sorted pumice lapilli breccia. In medial outcrops (e.g., MER229 and MER325), the deposit
390 shows two subunits with poorly developed normal grading. The componentry shows that
391 Ba-P5 contains 55-75% pumice clasts (55-75% microvesicular, ≤20% expanded and ≤1% tube
392 pumice), 5-40% free crystals (feldspar, aenigmatite, pyroxene, amphibole and Fe-Ti oxides)
393 in the finer fractions and ≤5% lithics (crystal-rich obsidian, altered lava and ignimbrite). The
394 pumice clasts are moderately vesicular (50-65% vesicularity) with <10% phenocrysts of alkali
395 feldspar, aenigmatite, orthopyroxene and amphibole, and a glassy groundmass. The Ba-P5
396 tephra deposit is interpreted as a fallout tephra unit. A bulk sample of this unit was
397 collected at section MER147 for single-crystal (alkali feldspar) $^{40}Ar/^{39}Ar$ dating, and yields an
398 age of 87 ± 16 (2σ) ka (Table 1).

399 Ba-P6 is a well-preserved Baricha deposit overlying Ba-P5 and separated from it by a
400 palaeosol. A maximum thickness of ~4 m is measured in a proximal gully section (MER302).
401 In most outcrops (e.g. MER205 and MER302), Ba-P6 shows dm-scaled multiple horizons of
402 well-sorted coarse to fine pumice lapilli with abrupt grain size transitions. The componentry
403 shows that Ba-P6 is almost lithic-free (≤2% of crystal rich obsidian, altered lava and
404 ignimbrite) and contains 50-70% pumice clasts (50-70% microvesicular and <10% expanded
405 pumice) and ca. 30% free crystals (feldspar, aenigmatite, amphibole and Fe-Ti oxides) in the
406 finer fractions below 1 mm. The pumice clasts are moderately vesicular (50% vesicularity),
407 with <10% phenocrysts of alkali feldspar, aenigmatite and amphibole, set in a glassy
408 groundmass. The depositional characteristics indicate that the Ba-P6 deposit is a tephra fall
409 deposit.

Ba-P7 is a light grey pumice deposit confirmed in 15 different stratigraphic sections. The unit is 5 m thick at 4 km distance from the summit (MER205). The bottom of Ba-P7 is a matrix-supported and cream-coloured pyroclastic deposit in medial outcrops (at ~15 km distance from the source) and a fallout unit in proximal outcrops. The main part of the Ba-P7 unit is diffusely dm-scale bedded, but overall normally graded and poorly sorted pumice lapilli breccia. In the upper half of the unit, pumice bombs up to 10-15 cm diameter are present. The componentry shows that Ba-P7 is almost lithic-free (≤2% of crystal rich obsidian, altered lava and ignimbrite) and contains 65-90% pumice clasts (65-85% microvesicular, ≤2% expanded and ≤2% tube pumice) and 5-30% free crystals (feldspar, aenigmatite and Fe-Ti oxides) in the finer fractions. The pumice clasts are moderately to highly vesicular (50-55% vesicularity), and almost aphyric with <1% phenocrysts of alkali feldspar and aenigmatite in a glassy groundmass. We interpret Ba-P7 as a PDC deposit (in medial outcrops) overlain by a tephra fall.

The youngest Baricha deposit found, Ba-P9, is a minor unit underlain by a cream-coloured, matrix-supported and undulatory bedded horizon that is interpreted as a PDC deposit. In outcrop MER308 a piece of black, friable charcoal was recovered from the upper part of this PDC deposit. A radiocarbon date of the charcoal yields an age of 1190 ± 36 cal yr BP (760 ± 36 CE).

In summary, at Baricha, we identify in total seven pumice fall deposits (Ba-P1, Ba-P3 to Ba-P8) and another two composite deposits that have both tephra fall and PDC units (Ba-P2 and Ba-P9; Table 2).

#### *4.1.4. Oda Sequence*

A sequence of pyroclastic deposits is exposed in the vicinity of the Oda crater and attributed to this centre. Oda has a well-developed 0.9 x 0.78 km crater partially filled by a small lake (Fig. 2a). The stratigraphic section to the SE of the summit crater (MER336) displays 8 different units with pantellerite-comendite glass compositions (Fig. 3). The tephra deposits are generally poorly preserved in medial and distal sites (>10 km). Two major (Od-P4 and Od-P5) and five minor units are assigned to Oda, each of them separated by poorly to well-developed palaeosols (Table 2).

Od-P4 is a pumice lapilli breccia deposit with cm-scale bedding and normal grading within each bed set in the bottom portion before becoming massive in the top ~30 cm. A maximum thickness of 3 m is observed in MER336. In several sections (e.g. MER231), the bottom 10-30 cm is marked by a lithic-rich poorly sorted ash-dominated horizon (i.e. tuff). The componentry shows that Od-P4 contains 60-80% pumice clasts (60-80% microvesicular and ≤1% tube pumice), ≤25% lithics (hydrothermally altered lava, glassy obsidian and ignimbrite) and 10-20% free crystals (feldspar, aenigmatite and Fe-Ti oxides) in the fractions below 1 mm. The pumice clasts are moderately to highly vesicular (55-65% vesicularity), and sparsely aphyric with ≤3% phenocrysts of alkali feldspar, clinopyroxene, amphibole and aenigmatite in a glassy to microlite-poor groundmass. The mineralogy of the microlites is similar to that of the phenocrysts. Od-P4 is interpreted as a PDC deposit overlain by a tephra fall.

Above Od-P4, a relatively well-preserved deposit (Od-P5) is exposed. Od-P5 is 3.5 m thick at Oda's flank and still ≥40 cm at 6 km distance (MER237) from the volcanic centre. The unit is characterised by a massive, fine pumice lapilli breccia, that is poorly sorted, lithic-rich and comprises few distinctly larger pumice clasts (~3.5 cm). The componentry shows that Od-P5 is lithic-poor (≤3% of hydrothermally altered lava and glassy obsidian) and contains 60-70%

pumice clasts (60-70% microvesicular and ≤1% tube pumice) and 5-35% free crystals (feldspar, quartz, aenigmatite, pyroxene, amphibole and Fe-Ti oxides) in the finer fractions. The depositional characteristics indicate that Od-P5 is a tephra fall deposit.

### *4.1.5. Bora Sequence*

Bora deposits are generally poorly preserved and found in the south western part of the BBTM complex. A deep gully (MER231) located at 11 km southwest of the Bora edifice exposes two major and one minor deposit with pantelleritic-comenditic compositions (Table 2, Fig. 4d). The pyroclastic deposits can be correlated with outcrops that extend to at least 14 km distance from the summit. The Bora sequence lies entirely on top of the Oda sequence and can be distinguished from the latter by its lithic-poor nature and rare hydrothermally altered lithics.

Bo-P2 is exposed in only a few proximal outcrops. The unit is a cm-scale bedded, well-sorted pumice lapilli breccia, and contains occasional pumice bombs (~15 cm in diameter). The deposit appears light grey at the base, and gradually progresses to a cream-coloured, lenticular-bedded, poorly sorted unit with sub-rounded pyroclasts towards the top. A maximum thickness of 2.5 m is observed in outcrop (MER231) located 11 km from the vent. The componentry of Bo-P2 shows 60% pumice (60% microvesicular and 1% tube pumice), ≤15% free crystals (feldspar, quartz and Fe-Ti oxides) in the finer fractions and <8% lithics (hydrothermally altered lava, glassy obsidian and ignimbrite). The pumice clasts are entirely aphyric and moderately vesicular (ca. 60% vesicularity). We interpret the lower half portion of Bo-P2 to be formed by tephra fall and the upper portion to result from the main unit's weathering.

Bo-P3 is a relatively widespread Bora deposit. The unit is an entirely massive, poorly sorted coarse pumice lapilli breccia. The maximum thickness of the deposit is 3 m and thins out to a minimum of 65-70 cm in medial outcrops at 13 km distance from the summit. The componentry of Bo-P3 shows it to be almost lithic-free (≤1% altered lava and glassy obsidian), and contain 90% pumice (80% microvesicular, 5% expanded and 3% tube pumice) and 5% free crystals (feldspar, aenigmatite, pyroxene and Fe-Ti oxides) mainly concentrated in the finer fractions. The pumice clasts are almost aphyric (<0.5% alkali feldspar, aenigmatite and orthopyroxene), moderately to highly vesicular (45-75% vesicularity), and have a glassy groundmass. The depositional characteristics suggest that Bo-P3 is a pyroclastic fall deposit.

#### *4.1.6. Werdi Sequence*

Werdi deposits are exposed in a few outcrops located in the central and northern parts of the volcanic complex. A gully section (MER309; Fig. 4e) located in the vicinity of the southern Lake Koka shore provides an apparently near complete overview of the Werdi sequence. At MER309 three Werdi units, 2 major (Wd-P1 and Wd-P2) and 1 minor (Wd-P3; Table 2), are observed. The Werdi sequence overlies the Suke deposits and is separated from it by well-developed palaeosols. The Werdi deposits are easily identified by the bluish-grey colour of the pumice clasts and pantelleritic-comenditic compositions.

Wd-P1 sits stratigraphically above the Suke deposit (MER309) and an obsidian lava flow (MER246). The unit is bedded at the cm-scale, poorly sorted, lithic-poor and composed of coarse ash to pumice lapilli. Wd-P1 has a maximum thickness of 15 m and contains occasional pumice bombs (~10 cm) in very proximal outcrops. Wd-P1 contains ca. 83%

bluish-grey pumice (microvesicular), ca. 10% lithics (hydrothermally altered lava and crystal-rich obsidian), and ca. 5% free crystals (feldspar, aenigmatite, pyroxene and amphibole) in the grain size fractions below 4 mm. Wd-P1 likely originates from a tephra fall.

Wd-P1 is overlain by another 35 cm thick Werdi unit (i.e. Wd-P2) in the MER309 outcrop. In outcrop MER246, Wd-P2 is underlain by crystal-rich obsidian lava. The unit appears as a lithic-poor, well-sorted and massive coarse pumice lapilli breccia. In section MER245 the top part of this unit shows normal grading. The componentry of Wd-P2 shows it to be almost lithic-free (<5% altered lava, glassy obsidian and ignimbrite), with ca. 70% bluish-grey pumice (microvesicular) and ca. 20% free crystals (feldspar, aenigmatite and Fe-Ti oxides) in the finer fractions. The pumice clasts are almost aphyric (ca. 1% alkali feldspar and aenigmatite), moderately vesicular (50% vesicularity), and have a glassy groundmass. The depositional characteristics indicate that Wd-P2 represents a pyroclastic fall.

#### *4.1.7. Tullu Moye Sequence*

Tullu Moye deposits are exposed in the heavily faulted eastern zone of the volcanic complex. Two different Tullu Moye units are identified above well-developed palaeosols in most outcrops. Both units are characterised by their distinct white pumice clasts of comenditic composition. TM-P2 is the youngest and main Tullu Moye deposit that overlies TM-P1 (Table 2). The two units are separated by a palaeosol (MER152), but in some proximal outcrops an 80 cm thick scoria lapilli (interpreted as a fall) deposit is interbedded between the two pumice horizons. TM-P2 is widespread to the West and has a maximum thickness of 2 m in proximal outcrops (e.g. MER240). TM-P2 is a massive, poorly sorted pumice lapilli breccia, and contains occasional pumice bombs (up to 15 cm). The deposit is

almost lithic-free (<3% hydrothermally altered lava and glassy obsidian), and contains ca. 70-100% white pumice (70-100% microvesicular, ≤1% expanded and ≤1% tube pumice) and ≤20% free crystals (feldspar, pyroxene, amphibole and Fe-Ti oxides) in the finer fractions. The pumice clasts are almost aphyric (ca. 2% alkali feldspar, clinopyroxene and amphibole), moderately vesicular (60% vesicularity), and have a glassy groundmass.

### *4.1.8. Additional deposits*

Besides the well-dispersed BBTM tephra deposits described in sections 4.1.1 to 4.1.7, a significant number of deposits are found in single outcrops without having a correlative in other sites. Most of these deposits are exposed on the flanks of monogenetic pumice cones. At least 11 separate vent / cones are identified around the larger edifices such as Bora, Baricha and Tullu Moye (Fig. 2a). These are interpreted as pumice cones which are also common at Aluto volcano (e.g. Clarke et al. 2020). The maximum thickness of the deposits ranges from <1 m to 8 m. These deposits are characterised by massive, poorly sorted pumice lapilli breccia with occasional pumice bombs (up to 8 cm in diameter) and expanded pumice clasts. The deposits identified at outcrops MER209 and MER150 shows an alternation of tephra layers with relative variations of sorting and stratification. The lab-based componentry analysis shows that these deposits contain 70-95% pumice clasts (60-90% microvesicular, ≤10% expanded and <10% tube pumice), <25% lithics (altered lava, glassy obsidian and ignimbrite) and <20% free crystals (feldspar, quartz, aenigmatite and Fe-Ti oxides) in the finer fractions. The pumice clasts are rhyolitic in composition, moderately vesicular (ca. 35-60% vesicularity) and almost aphyric (<3%).

In addition to these units attributed to pumice cones, there are some other deposits observed in the BBTM volcanic complex that also have no correlatives. At least seven tephra deposits are identified in the regions around Baricha, Oda and Tullu Moye. At MER201, near the Baricha edifice, two massive pumice lapilli breccia layers have thicknesses of 1.3 m and ~2 m, but have not been identified elsewhere. At section MER 237, three relatively thin (max. 40 cm), massive, lithic-poor fine lapilli breccia units alternate with a reworked pyroclastic deposit. In the eastern rift escarpment, at MER 385, ~6 km E of Tullu Moye, two tephra layers with pantellerite-comedite compositions are found. The field data and componentry of these deposits are distinct from those of any BBTM major units.

## 4.2. Glass chemistry

### 4.2.1. Major element composition

Major element glass compositions of selected proximal, medial and distal tephra (pumice) deposits from the BBTM region reveal that the parental melts consistently have alkali-rich rhyolite compositions (Fig. 6a). The average major element compositions of the selected tephra deposits are presented in Table 3, with the full dataset in Supplementary information (SM-2). All compositions are peralkaline and are classified as either pantellerite or comendite (Fig. 6b). The latter composition is characteristic of Tullu Moye tephra only, whereas all deposits from Baricha, Suke and Meki are entirely pantelleritic. The glass compositions of Oda, Werdi and Bora tephra deposits, straddle the comendite-pantellerite boundary (Fig. 6b). Except for the distinct comenditic Tullu Moye glasses, all BBTM glass major element compositions overlap with those of Aluto, Corbetti and Gedemsa tephra deposits (Fig. 6, 7; Martin-Jones et al. 2017; Fontijn et al. 2018; McNamara et al. 2018).

570 Each pantelleritic deposit has a tight homogeneous composition within the larger
571 pantellerite cluster (70.1-77.9 wt% $SiO_2$, 6.0-14.8 wt% TA; 7.6-11.7 wt% $Al_2O_3$, 4.3-7.3 wt%
572 FeO). However, different deposits may overlap in composition, complicating correlations
573 based on major element glass composition alone. In general, Baricha deposits tend to have
574 the highest Total Alkali and FeO contents and are also distinct in other major element
575 contents, e.g., $TiO_2$ (Fig. 7b). Meki and Suke tephra predominantly have glass compositions
576 with a higher $TiO_2$ (>0.23 wt%) and CaO (>0.2 wt%) content relative to those of Baricha.
577 Meki and Suke are also distinguished from each other, especially by their $Al_2O_3$ and FeO
578 contents (Fig. 6b, 7a-d). There are no discernible chemical differences between the
579 individual Baricha tephra units.

580 The Tullu Moye pyroclastic deposits are mainly composed of comenditic glass. This tephra
581 group is slightly less evolved (lower $SiO_2$) compared to the other BBTM tephra deposits. It is
582 characterized by a lower amount of $SiO_2$ (71.3-73.6 wt%), FeO (1.6-3.5 wt%) and a distinctly
583 higher amount of $Al_2O_3$ (12.4-15.1 wt%; Fig. 6). These two Tullu Moye deposits (TM-P1 and
584 TM-P2) each also have highly distinct glass compositions, as revealed by their separate
585 clusters in all major element bivariate diagrams (Fig. 6-7). TM-P1 is characterised by a higher
586 TiO2, $Al_2O_3$, CaO, $K_2O$ (Fig. 7) and MgO (not plotted) contents relative to TM-P2. TM-P2 is
587 relatively more evolved than TM-P1 and contains higher contents of $SiO_2$, $Na_2O$ and FeO
588 (Fig. 6-7).

589 The tephra deposits from Oda, Werdi and Bora show significant compositional
590 heterogeneity in the glass major element composition. The melt compositions span from
591 comenditic to pantelleritic and many fall near the compositional divide on the peralkaline
592 classification diagram (Fig. 6b). Many samples in this population overlap with the highly

593 evolved (high-$SiO_2$) end of the pantelleritic rhyolites. The FeO and $Al_2O_3$ contents can be
594 used to discriminate some of the tephra units in this population. For example, glasses from
595 Od-P1, Od-P2, Od-P3, Od-P4 and Wd-P2 have slightly lower FeO (<5 wt%) and higher $Al_2O_3$
596 (>9.1 wt%) contents than the other samples in this group. In contrast, deposits such as Od-
597 P7, Wd-P3 and Wd-P1 have higher FeO (>~6 wt%) and lower $Al_2O_3$ (<9 wt%) contents. The
598 other tephra units in this population show a wide variation of FeO (3.9-7 wt%) and $Al_2O_3$
599 (7.8-11 wt%) contents. The other major element contents like silica and the total alkali
600 contents show less variation (Fig. 6a). One uncorrelated tephra unit exposed at MER150
601 shows a similar (comenditic) composition to Oda and Werdi deposits (Fig. 6-7). The field,
602 componentry and petrographic data show that this MER150 tephra is likely sourced from a
603 small pumice cone located in the SW part of the complex. In this deposit, there is a strikingly
604 clear chemical variation from comendite to less evolved pantellerites through the
605 stratigraphy.

606

607 **4.2.2. Trace element composition**

608 To investigate the compositional variability of the BBTM tephra deposits in more detail,
609 trace element glass data were obtained on a selection of samples already analysed by
610 EPMA. The average glass trace element compositions of the analysed tephra layers are
611 presented in Table 3, with the full dataset in Supplementary information (SM-5). The
612 geochemical group revealed by the major element data (section 4.2.1) are also evident in
613 the trace element compositions (Fig. 8). The pantelleritic samples (e.g. Baricha) have
614 systematically higher concentrations of incompatible trace elements (e.g. Zr, Rb, Y, La, Ce)
615 than the comendites (e.g. Tullu Moye). The trace element glass data further highlight

significant compositional variation within the pantellerite population between Baricha and the other tephra deposits (Fig. 8). Baricha glasses have higher Zr (>1500 ppm), Rb (>200 ppm), Y (>150 ppm), La (>150 ppm) and Ce (>300 ppm) contents relative to those from Oda, Suke, Meki and Bora. Other trace elements such as Nb, Cs, Pb and other REEs are also more enriched in the Baricha samples. The only analysed trace elements that are depleted in the pantellerites relative to the comendites are Ba and Sr. The Ba and Sr contents indicate, again, that the oldest Tullu Moye unit (TM-P1; Ba: 550 ± 50 ppm and Sr: 50 ± 10 ppm) is compositionally distinct from the youngest unit (TM-P2; Ba: 400 ± 50 ppm and Sr: 10 ± 3 ppm) (Fig. 8).

Unlike the major element compositions, Aluto tephra trace element compositions (McNamara et al. 2018) show distinct differences with those of Baricha, Meki and Suke samples, especially in Ba and REE content (Fig. 8).

### 4.3. Eruptive Volume and Magnitude

The tephra fall volume for 12 major eruptions is estimated by manually constructing isopach maps (Fig. 9). Unfortunately, the Suke, Meki and 13 post-caldera deposits are not sufficiently exposed over multiple locations to provide an estimate on volume. Two deposits (Ba-P4 and Ba-P5) were identified in multiple locations covering a large enough area so that more than two isopach contour lines could be constructed (Fig. 9a-b). We calculated the minimum bulk deposit volume for these two deposits using the 1-segment exponential thickness decay model of Pyle (1989). The limited exposure does not allow multiple segments to be identified on a thickness-area trend (Bonadonna et al. 1998) and thus other methods to estimate deposit volume, typically requiring additional constraints (e.g.

639 Bonadonna & Houghton 2005), are not suitable in this case. For the 10 remaining deposits
640 identified in multiple locations (Ba-P2, Ba-P3, Ba-P6, Ba-P7, Od-P4, Od-P5, Wd-P2, Wd-P1
641 and TM-P2), only one or two contour lines can be inferred, and for these we use the Legros
642 (2000) one-isopach method to estimate their minimum bulk volume. The bulk volume
643 estimation of these deposits falls in the range 0.007 $km^3$ to 1.1 $km^3$. The componentry data
644 of these deposits indicates the lithic content is very low (<10% in the fraction below 4 mm)
645 compared to the juvenile proportion. Therefore, we only considered the pumice when
646 converting the bulk deposit volume to a dense rock equivalent (DRE) volume, by assuming
647 2300 $kg/m^3$ rhyolite melt density (Fierstein & Hildreth 1992) and 470 $kg/m^3$ average bulk
648 density as measured on BBTM deposits. The DRE volume of major BBTM eruptions is thus
649 estimated between 0.001 $km^3$ to 0.22 $km^3$. These estimates were then used to calculate
650 minimum magnitude of these eruptions using the following relationship: Magnitude = $\log_{10}$
651 [erupted mass, kg] - 7 (Pyle 2015). Based on the preserved deposits, most magnitude
652 estimates range from 3.9 to 4.7 for eruptions from Werdi, Oda, Bora and Baricha (see
653 supplementary material SM-6). The youngest Tullu Moye eruption however has a lower
654 minimum magnitude of 2.5. The three Baricha eruptions that are most widespread, up to 20
655 km west of the edifice (Ba-P4, Ba-P5 and Ba-P7) have a minimum estimated magnitude of
656 4.6 to 4.7.

657

658 **5. Discussion**

659 **5.1. Tephrostratigraphy and Correlation**

660 Eruptive deposits from the BBTM volcanic complex overlay a series of older volcanic rocks
661 (Fig. 2b). The base of the BBTM sequence observed in the field (this work) and in shallow

662 wells (Ayele et al. 2002) comprises welded ignimbrite and lavas of different composition
663 (rhyolite, trachyte and basalt). This series blankets the rift floor and in different parts of the
664 MER is known as the Nazret unit (Kazmin & Berhe 1978). An obsidian flow and ignimbrite of
665 this series collected near Tullu Moye volcano yields a late Pleistocene age of 1.58 ± 0.2 Ma
666 (WoldeGabriel et al. 1990) which is coeval to the development of the Wonji Fault Belt (WFB)
667 along the MER axis (1.6 Ma; Ebinger & Casey 2001). This older unit is related to pre-BBTM
668 volcanism and may be associated with the start of tectono-magmatic focusing along the
669 axial zone of the MER.

670 The oldest deposit recognised in our work, the Suke deposit, is primarily composed of large
671 boulders and blocks of poorly-vesiculated pumice and obsidian lithics at the type section
672 (MER253; Fig. 2). A few kilometres SE from the type section, this unit becomes finer-grained
673 with a more prominent ashy matrix. We interpret the Suke deposit as an unwelded
674 ignimbrite unit, with its very coarse facies a “pumice and lithic lag breccia”, commonly
675 interpreted to represent the onset of caldera collapse (e.g. Druitt & Sparks 1982; Jordan et
676 al. 2018; Seggiaro et al. 2019). The dense and coarse blocks, possibly partially related to
677 vent erosion or widening, thus segregated from the PDCs which then carried relatively finer
678 material further from the source (Druitt & Sparks 1982; Druitt 1985; Walker 1985). The
679 juvenile volcanic products have no datable material (i.e. sanidine) and thus the absolute age
680 of the Suke caldera-forming event remains unconstrained.

681 The Meki deposit directly overlays deposits of the Suke caldera-forming eruption. A faint
682 weathered horizon at the top of the Suke deposits indicates a hiatus and testifies that the
683 two units represent different eruptions. The glass compositions further support this
684 interpretation, with a clear difference in $Al_2O_3$ and FeO contents between the two deposits

(Fig. 6b, 7a-d). The Meki deposit is a very thick fall (>20 m; cumulative of at least two horizons) and PDC (>13 m) deposit at 20-25 km distance from the centre of BBTM volcanic complex. At these medial locations (20-25 km from the vent) three main distinct horizons are observed in the Meki deposit. These horizons are massive tephra fall at the base and top, separated by alternating tephra fall and poorly sorted PDC deposits. Across this sequence, the deposits are characteristically lithic-free, which can be partially used as a diagnostic feature to identify them in the field. The brown surficial staining on the pumice deposits at ca. 1660 m asl. and the deposits age (107.7 ± 8.8 ka) suggest that the Meki eruption possibly pre-dates with the lake-level high stand of the oldest megalake phase that covered most of the Central MER (Benvenuti et al. 2002), including the western portion of the BBTM volcanic system.

Despite the lithic-free nature of the deposits, and relative limited exposure preventing volume estimates, the large thickness of the deposits and distance to the source, leads us to suggest that the Meki eruption may have led to another caldera collapse. Other volcanic complexes in the Central MER had caldera-forming eruptions at 180 ± 30 ka (Corbetti), 306 ± 12 to 316 ± 19 ka (Aluto) and 282 ± 110 ka (Gedemsa; Hutchison et al. 2016a, b). The 107.7 ± 8.8 ka Meki eruption may thus be the youngest caldera-forming event in the central sector of the MER, and is also notably younger than the hypothesised ignimbrite flare-up window (320 to 170 ka) proposed by Hutchison et al. (2016b). Additional age constraints on Central MER caldera-forming eruptions, such as the Suke ignimbrite, are required to test the flare-up hypothesis. Due to extensive post-caldera activity, the dimensions and geometry of the inferred caldera associated with the large Suke and Meki eruptions are difficult to trace. However, there are some possible remnants visible on the hill-shade map on Figure 2a and

noted by Korme et al. (2004) as “Tullu caldera” that requires further study to establish any association with the large eruptions documented here.

As reported in several case studies, caldera-forming eruptions may experience a transition from a single-vent phase to a subsidence-related multiple vent phase along a ring structure in the post-caldera sequence of events (e.g. Druitt & Sparks 1984; Lipman 1984; Heiken & McCoy 1984; Hildreth & Mahood 1986). The BBTM experienced both effusive and explosive volcanism during its post-caldera stage, forming both lavas and pyroclastic deposits (Di Paola 1972; Fontijn et al. 2018; this work). The widespread tephra deposits were identified to originate from the Baricha, Bora, Oda, Werdi and Tullu Moye edifices (section 4.1). In proximal sequences, we find deposit characteristics, such as the presence of ballistics, expanded clasts, coarse-grained pumice and lithic breccias. The stratigraphic relationship between the caldera-forming and post-caldera deposits can be observed in some sections, with palaeosols developed on top of the former, indicating a hiatus. One post-caldera eruption in the Baricha sequence (Ba-P5) was dated at 87 ± 16 ka and is underlain by at least 4 more post-caldera eruptions. The pause in volcanic activity following the youngest caldera-forming eruption (Meki) is thus at most on the order of thousands to a few tens of thousands of years at BBTM. This is distinctly shorter than the inferred 250 ky hiatus identified by Hutchison et al. (2016a) at Aluto following the caldera-forming event.

The Meki deposit is entirely lithic-free, whereas the post-caldera deposits contain some lithics. This may be related to a restructuring of the plumbing system caused by the caldera collapse (e.g. Hildreth & Mahood 1986), competence variation of rocks at fragmentation depth (Aravena 2017) and/or possible presence of a lithic-dominated deposit horizon other than the Meki one at depth. The lithic components in the post-caldera deposits are mainly

731 composed of green ignimbrite, rhyolite, basalt and obsidian lava. The subsurface geology of
732 BBTM, observed in the shallow drill cuttings (Ayele et al. 2002; Fig. 2b) shows an ignimbrite
733 and lava series similar to these lithic components. This may indicate that the lithic
734 components in the deposits are mainly sourced from vent erosion at a relatively deep level
735 (5-170 m).

736 The glass composition of Suke, Meki, Baricha and some Bora tephras are pantelleritic and
737 show a lot of similarities (e.g. 70-78 wt% $SiO_2$), even in the trace element contents. This
738 creates a practical complication for the correlation of the deposits based on glass chemistry
739 alone. This chemical homogeneity is commonly found in highly evolved tephra deposits (e.g.
740 Toba: Smith et al. 2011; Ciomadul: Harangi et al. 2020; Aeolian Islands: Albert et al. 2017;
741 Corbetti: Fontijn et al. 2018; Martin-Jones et al. 2017). Other characteristics, e.g.
742 componentry, are thus required to help correlate the units. Notably, the Baricha tephra
743 deposits are the only units that do not contain any lithics of hydrothermally altered reddish
744 lava, in stark contrast to the Bora units. In addition, the absence of lithics in Meki is
745 diagnostic and allows it to be distinguished from other BBTM deposits.

746 The pumice cone deposits that outcrop around the major centres likely represent relatively
747 small-scale eruptions. They are characterised by significant deposit thinning over short
748 spatial distance and fall-PDC successions consistent with alternating sustained columns and
749 plume collapses (Clarke et al. 2019).

750 The glass major element chemistry of the BBTM deposits overlaps with that of the Aluto and
751 Corbetti deposits. However, the trace element data, especially Ba and some REEs, differ and
752 can be used to discriminate BBTM from Aluto compositions. The generally higher

753 incompatible trace element concentrations of Meki indicate that the melt was more evolved
754 than at Aluto.

755

756 **5.2. BBTM Eruptive Frequency**

757 Based on the established tephrostratigraphic framework, we can constrain the overall
758 eruptive frequency of BBTM. BBTM experienced at least two caldera-forming eruptions, the
759 most recent one (Meki) at 107.7 ± 8.8 ka. After this eruption, post-caldera volcanic centres
760 such as Baricha, Bora, Oda, Werdi and Tullu Moye together erupted explosively at least 25
761 times within the last 100-116 ky and that left pyroclastic deposits that can be traced in
762 multiple locations. In addition, more than 7 non-correlated units are identified, each likely
763 representing a single eruption. Therefore, on average at least one explosive eruption
764 occurred per 3000-4000 years in the BBTM volcanic system. Of these post-caldera explosive
765 eruptions, three are attributed to Bora, eight to Oda, three to Werdi and two to Tullu Moye.
766 Additionally, Baricha volcano was the source of at least nine eruptions. For two Baricha
767 eruptions, we were able to constrain an absolute age: the Ba-P5 eruption occurred at 87 ±
768 16 ka and the Ba-P9 eruption (the youngest that is preserved in the record) occurred at
769 1190 ± 36 cal yr BP. This shows that Baricha had at least 5 eruptions within the first ca.
770 20,000 years after the Meki eruption and then at least 4 more eruptions since ca. 87 ka.
771 Since younger and/or larger eruption products are expected to be preferentially preserved
772 relative to older and/or smaller deposits (Brown et al. 2014), the geological records are may
773 be biased. The chronological (and magnitude) constraints on our present stratigraphic
774 framework are unfortunately too incomplete to allow inferring any changes in eruption
775 frequency or rate through time at BBTM. Our magnitude (Section 4.3) estimations suggest

776 that the BBTM volcanic complex has experienced at least 11 post-caldera explosive
777 eruptions with a magnitude of 4 or above (Section 4.3) within the last ca. 100,000 years.
778 Note that our evaluations of eruption frequency and magnitude do not take into account
779 the effusive eruptive products and are also based on minimum frequency and eruptive
780 volume estimations that are certainly influenced by deposit preservation and/or deposit
781 thinning behaviour (e.g. Bonadonna & Houghton 2005). Regardless, compared to other
782 volcanic complexes in the region, such as Aluto and Corbetti, BBTM seems less frequently
783 active in terms of explosive eruptions. However, BBTM may be more frequently active, and
784 characterised by higher-magnitude post-caldera eruptions, compared to the volcanic
785 systems located further north (e.g. Boset-Bericha and Fentale), which experienced several
786 effusive and a more limited number of explosive eruptions in their recent past (e.g. Fontijn
787 et al. 2018; Siegburg et al. 2018). The combined terrestrial and lacustrine records of Corbetti
788 tephra indicate an explosive eruption every ca. 700-1000 years (Fontijn et al. 2018; Martin-
789 Jones et al. 2017). The lacustrine record provides detailed constraints on the Holocene
790 eruptive history of the volcano by supplementing the terrestrial records (Martin-Jones et al.
791 2017). The Wendo Koshe Younger Pumice (WKYP) has an estimated minimum volume of 1.3
792 $km^3$ (Rapprich et al. 2016; Fontijn et al. 2018), or a magnitude of 4.8 using the same
793 approach as above. In the post-caldera phase, at least during the Holocene, Aluto had an
794 average of 3 eruptions per 1000 years (Martin-Jones et al. 2017; Fontijn et al. 2018;
795 McNamara et al. 2018). Considering the rapid thinning trend of the relatively well-
796 documented Qup deposit, Fontijn et al. (2018) roughly estimated a magnitude of 3 for this
797 pumice cone eruption. There is very little information regarding eruption magnitude for
798 other volcanoes in the MER to make a quantitative comparison. However, from the

799 available information (WKYP: M=4.8 and Qup: M~=3) we conclude that BBTM has eruptions
800 of at least comparable magnitude than Corbetti and Aluto in their post-caldera phase.

801

802 **5.3. Hazard Implications**

803 The tephrostratigraphic record of BBTM provides evidence for at least two major caldera-
804 forming events and 25 moderate-scale explosive eruptions. The spatial distribution of the
805 deposits of caldera-forming eruptions is poorly constrained because of the abundant post-
806 caldera deposits that conceal them. The second caldera-forming eruption, Meki, has better
807 exposures that document its tephra dispersion. This eruption deposited >20 m tephra fall
808 and >13 m PDCs at medial locations, and >1.1 m tephra fall at distal regions. The established
809 frequency-magnitude information in section 5.1 indicates an explosive eruption occurs from
810 BBTM at least every 3000-4000 yrs. The isopach maps of the well-dispersed post-caldera
811 deposits (Ba-P4 and Ba-P5) indicate dispersion of tephra up to at least 20 km from the
812 volcanic centre, for example in the town of Alem Tena, where deposits are still 1 m thick.
813 These eruptions also accumulated up to 5 m thick deposits in the proximal exposures
814 located within 4 to 5 km of the vent. Oda emplaced clast-supported to matrix-supported
815 PDCs during the penultimate identified eruption (Od-P7). This deposit is identified in a valley
816 that was formed by an intermittent stream that feeds Ziway Lake. Near the base of the Oda
817 edifice, it is 16 m thick and 10 km away it still is 1.5 m thick. In general, from the spatial
818 distribution of the pyroclastic deposits, we can conclude that several BBTM eruptions
819 covered a surface with a radius of at least 25 km.

820 Within this 25 km radius from any of the main centres, there are numerous urban and rural
821 settlements with highly variable population densities (Fig. 2a). The towns of Alem Tena (10

822 km from Baricha), Meki (20 km from Bora), Ogolcho (12 km from Oda) and Iteya (11 km
823 from Tullu Moye) are all located within this radius from at least one of the main volcanic
824 vents. Total estimates of around one hundred thousand people are living in these towns and
825 the surrounding rural areas, with many of them highly dependent on agriculture (CSAE
826 2007). In the towns, with the exception of Iteya, 1 to 20 m thick tephra fall has been
827 deposited during past eruptions. The area is also exposed to tephra fall hazard in the future,
828 and this could cause a major threat to human health and livelihoods, buildings and other
829 infrastructure, economic activities, and ecosystems (e.g. Spence et al. 2005; Wilson et al.
830 2012). To the West of Meki and Ogolcho, PDC deposits with thicknesses between 1.5 to 13
831 m also indicate an additional potential volcanic hazard to the BBTM region.

832 Detailed volcanic hazard assessments can be useful for land-use planning and development
833 of mid-to-long-term risk mitigation strategies. Volcanic hazard maps are often to a large
834 extent based on a volcano's past eruptive history (e.g. Calder et al., 2015). Our current data
835 provide some initial constraints on frequency and magnitude of past eruptions at BBTM, the
836 extent of volcanic deposits inundation and possible related volcanic hazards to the nearby
837 region. Given the high population density and presence of critical infrastructure (e.g. Tullu
838 Moye geothermal facilities) our results may be used as a background for future research in
839 the direction of generating more detailed, potentially probabilistic, volcanic hazard
840 assessment (e.g. Clarke et al. 2020; Tierz et al. 2020) or volcano monitoring activities.

841

842 **6. Conclusion**

843 A detailed study on the tephrostratigraphic framework of the BBTM tephra deposits has
844 enabled us to reconstruct the past explosive activity of the volcanic complex. Here we

845 present the first detailed stratigraphic record of the explosive eruptions experienced in the
846 BBTM volcanic complex. The field data, glass chemistry (major and trace elements),
847 componentry and petrographic data allow us to identify 27 eruptions that include pumice
848 fall and/or PDC deposits. The first two tephra deposits are associated with two different
849 caldera-forming eruptions: the (1) Suke caldera deposits that are characterized by a lag
850 breccia lithofacies and (2) Meki caldera eruption, represented by a very thick tephra fall and
851 flow succession with an age of 107.7 ± 8.8 (2σ) ka ($^{40}Ar/^{39}Ar$). This new age of the Meki
852 tephra reveals it to be the youngest caldera-forming eruption identified in the Central MER
853 so far. During the post-caldera volcanism, the BBTM underwent at least 25 moderate-major
854 eruptions sourced from Baricha (9), Bora (3), Oda (8), Werdi (3) and Tullu Moye (2) edifices.
855 The melts that formed these deposits are categorized as comenditic (Tullu Moye) and
856 pantelleritic rhyolites based on the major element glass chemistry. The trace element data
857 indicates that the BBTM pantelleritic tephra are more evolved than those of Aluto volcano
858 located to the south of the study area. The componentry of these deposits reveals a
859 significant variation in pumice, lithics and free mineral content within the deposits. The
860 pumice has a very low percentage of phenocrysts (<10%).

861 When we consider the BBTM post-caldera phase only, the recurrence rate of the explosive
862 activity from this extended volcanic system is ≥1 eruption per 4000 yrs. This explosive
863 eruption frequency is much lower compared to Aluto and Corbetti, which has been
864 reconstructed from both terrestrial and lacustrine records. The estimated tephra volume for
865 the well exposed units indicates eruption magnitudes pre-dominantly varying from 4 to 5.
866 Only at Tullu Moye deposits of smaller (magnitude 2.5) eruptions were identified in the
867 geological record. For most of the larger eruptions, tephra was dispersed up to 20 km from

868 the volcanic centre suggesting that more than hundred thousand people could be affected
869 by future eruptions of similar magnitude in this area.

870

871 **Acknowledgements**

872 AT is supported by the F.R.S.-FNRS Aspirant doctoral fund. Several samples and an extensive
873 glass chemistry dataset were collected under the NERC-funded RiftVolc Large Grant
874 (NE/L013649/1) by KF along with others. We would like to thank Tamsin Mather and David
875 Pyle for giving the permission to access the dataset and samples from the RiftVolc project.
876 KF further acknowledges support from F.R.S.-FNRS MIS grant F.4515.20. The iCRAG LA-ICP-
877 MS facility at Trinity College Dublin is supported by SFI award 13/RC/2092. Field work and
878 sample export was kindly permitted by authorities of the Oromia region and Ministry of
879 Mines and Petroleum of Ethiopia, respectively. Professional logistical support was provided
880 by Ethioder Pvt Ltd Co and their drivers. Mathieu Boudin (KIK-IRPA, Institut Royal du
881 Patrimoine Artistique) handled the radiocarbon dating. We thank Thomas Gernon and one
882 anonymous reviewer for detailed and constructive comments which improved the paper.

883

884 **Reference**

885 Agostini, A., Bonini, M., Corti, G., Sani, F. and Mazzarini, F., 2011. Fault architecture in the
886 Main Ethiopian Rift and comparison with experimental models: implications for rift
887 evolution and Nubia–Somalia kinematics. Earth and Planetary Science Letters, 301(3-
888 4): 479-492.

889 Albino, F. and Biggs, J., 2021. Magmatic Processes in the East African Rift System: Insights
890 From a 2015–2020 Sentinel-1 InSAR Survey. Geochemistry, Geophysics, Geosystems,
891 22(3): e2020GC009488.

892 Albert, P. G., Tomlinson, E. L., Smith, V. C., Di Traglia, F., Pistolesi, M., Morris, A.,Donato, P.,
893 De Rosa, R., Sulpizio, R., Keller, J. and Rosi, M., 2017. Glass geochemistry of pyroclastic
894 deposits from the Aeolian Islands in the last 50 ka: a proximal database for
895 tephrochronology. Journal of Volcanology and Geothermal Research, 336: 81-107.

896 Aravena, A., 2017. Stability of volcanic conduits: Critical mechanical parameters. Il nuovo
897 cimento C, 40(2): 1-9.

898 Aspinall, W. P., Auker, M., Hincks, T., Mahony, S., Nadim, F., Pooley, J., Sparks, R.S.J. and
899 Syre, E., 2011. Volcano hazard and exposure in GFDRR priority countries and risk
900 mitigation measures. Volcano Risk Study 0100806-00-1-R. Global Facility for disaster
901 Reduction and Recovery, Washington, D.C.

902 Ayele, A., Teklemariam, M.and Kebede, S., 2002. Geothermal exploration in the Abaya and
903 Tulu Moye-Gedemsa prospects, Main Ethiopian Rift. Geological Survey of Ethiopia,
904 Addis Ababa, 79 pp.

905 Balestrieri, M. L., Bonini, M., Corti, G., Sani, F. and Philippon, M., 2016. A refinement of the
906 chronology of rift-related faulting in the Broadly Rifted Zone, southern Ethiopia,
907 through apatite fission-track analysis. Tectonophysics, 671: 42-55.

908 Bastow, I. D., Keir, D. and Daly, E., 2011. The Ethiopia Afar Geoscientific Lithospheric
909 Experiment (EAGLE): Probing the transition from continental rifting to incipient
910 seafloor spreading. Volcanism and evolution of the African lithosphere, 478: 1-26.

911 Benvenuti, M., Carnicelli, S., Belluomini, G., Dainelli, N., Di Grazia, S., Ferrari, G. A., Lasio, C.,
912 Sagri, M., Ventra, D., Atnafu, B. and Kebede, S., 2002. The Ziway–Shala lake basin
913 (main Ethiopian rift, Ethiopia): a revision of basin evolution with special reference to
914 the Late Quaternary. Journal of African Earth Sciences, 35(2): 247-269.

915 Benvenuti, M., Bonini, M., Tassi, F., Corti, G., Sani, F., Agostini, A., Manetti, P and Vaselli, O.,
916 2013. Holocene lacustrine fluctuations and deep CO2 degassing in the northeastern
917 Lake Langano Basin (Main Ethiopian Rift). Journal of African Earth Sciences, 77: 1-10.

918 Biggs, J., Bastow, I. D., Keir, D. and Lewi, E., 2011. Pulses of deformation reveal frequently
919 recurring shallow magmatic activity beneath the Main Ethiopian Rift. Geochemistry,
920 Geophysics, Geosystems, 12(9).

921 Bizouard, H. and Di Paola, G. M., 1978. Mineralogy of the Tullu Moje active volcanic area
922 (Arussi: Ethiopian Rift valley). In Petrology and Geochemistry of Continental Rifts (pp.
923 87-100). Springer, Dordrecht.

924 Bonadonna, C., Ernst, G. G. J. and Sparks, R. S. J., 1998. Thickness variations and volume
925 estimates of tephra fall deposits: the importance of particle Reynolds number. Journal
926 of Volcanology and Geothermal Research, 81(3-4): 173-187.

927 Bonadonna, C. and Houghton, B. F., 2005. Total grain-size distribution and volume of tephra-
928 fall deposits. Bulletin of Volcanology. 67(5): 441-456.

929 Bronk Ramsey, C., 2009. Bayesian analysis of radiocarbon dates. Radiocarbon 51, 337e360.

930 Brown, S. K., Crosweller, H. S., Sparks, R. S. J., Cottrell, E., Deligne, N. I., Guerrero, N. O.,
931 Hobbs, L., Kiyosugi, K., Loughlin, S.C., Siebert, L. and Takarada, S., 2014.
932 Characterisation of the Quaternary eruption record: analysis of the Large Magnitude

933 Explosive Volcanic Eruptions (LaMEVE) database. Journal of Applied Volcanology, 3(1):
934 1-22.

935 Cas, R., Porritt, L., Pittari, A. and Hayman, P., 2008. A new approach to kimberlite facies
936 terminology using a revised general approach to the nomenclature of all volcanic rocks
937 and deposits: descriptive to genetic. Journal of Volcanology and Geothermal Research,
938 174(1-3): 226-240.

939 Calder, E.S., Wagner, K. and Ogburn, S.E., 2015. Volcanic hazard maps. In: Loughlin, S.C.,
940 Sparks, R.S.J., Brown, S.K., Jenkins, S.F., Vye-Brown, C. (eds). Global volcanic hazards
941 and risk, Cambridge. Cambridge University Press, 335-342.

942 Central Statistical Agency of Ethiopia (CSAE), 2007. The 2007 Population and Housing Census
943 of Ethiopia: Statistical Report for Oromiya Region; Part I: Population Size and
944 Characteristics. Report, Addis Ababa, Ethiopia.

945 Clarke, B., Calder, E. S., Dessalegn, F., Fontijn, K., Cortés, J. A., Naylor, M., Butler, I.,
946 Hutchison, W. and Yirgu, G., 2019. Fluidal pyroclasts reveal the intensity of peralkaline
947 rhyolite pumice cone eruptions. Nature communications, 10(1): 1-10.

948 Clarke, B. A., Tierz, P., Calder, E. S. and Yirgu, G., 2020. Probabilistic volcanic hazard
949 assessment for pyroclastic density currents from pumice cone eruptions at Aluto
950 volcano, Ethiopia. Frontiers in Earth Science, 348.

951 Daly, E., Keir, D., Ebinger, C. J., Stuart, G. W., Bastow, I. D. and Ayele, A., 2008. Crustal
952 tomographic imaging of a transitional continental rift: the Ethiopian rift. Geophysical
953 Journal International, 172(3): 1033-1048.

954 Di Paola, G. M., 1972. The Ethiopian Rift Valley (between 7 00’ and 8 40’ lat. north). Bulletin
955 Volcanologique, 36(4): 517-560.

956 Donovan, A. and Oppenheimer, C., 2012. Governing the lithosphere: insights from
957 Eyjafjallajökull concerning the role of scientists in supporting decision-making on
958 active volcanoes. Journal of Geophysical Research: Solid Earth, 117(B3).

959 Druitt, T. H., 1985. Vent evolution and lag breccia formation during the Cape Riva eruption
960 of Santorini, Greece. The Journal of Geology, 93(4): 439-454.

961 Druitt, T. H. and Sparks, R. S. J., 1982. A proximal ignimbrite breccia facies on Santorini,
962 Greece. Journal of Volcanology and Geothermal Research, 13(1-2): 147-171.

963 Druitt, T. H. and Sparks, R. S. J., 1984. On the formation of calderas during ignimbrite
964 eruptions. Nature, 310(5979): 679-681.

965 Ebinger, C., 2005. Continental break-up: the East African perspective. Astronomy &
966 Geophysics, 46(2): 2-16.

967 Ebinger, C. J., Yemane, T., Harding, D. J., Tesfaye, S., Kelley, S. and Rex, D. C., 2000. Rift
968 deflection, migration, and propagation: Linkage of the Ethiopian and Eastern rifts,
969 Africa. Geological Society of America Bulletin, 112(2): 163-176.

970 Ebinger, C. J. and Casey, M., 2001. Continental breakup in magmatic provinces: An Ethiopian
971 example. Geology, 29(6): 527-530.

972 Electroconsult (ELC), 1978. Geothermal reconnaissance study of selected sites of the
973 Ethiopian rift system. Geological report, Milano, Italy.

974 Fierstein, J. and Hildreth, W., 1992. The plinian eruptions of 1912 at Novarupta, Katmai
975 national park, Alaska. Bulletin of Volcanology, 54(8): 646-684.

976 Fontijn, K., McNamara, K., Tadesse, A. Z., Pyle, D. M., Dessalegn, F., Hutchison, W., Mather,
977 T.A. and Yirgu, G., 2018. Contrasting styles of post-caldera volcanism along the Main
978 Ethiopian Rift: Implications for contemporary volcanic hazards. Journal of Volcanology
979 and Geothermal Research, 356: 90-113.

980 Froggatt, P. C., 1983. Toward a comprehensive Upper Quaternary tephra and ignimbrite
981 stratigraphy in New Zealand using electron microprobe analysis of glass shards.
982 Quaternary research, 19(2): 188-200.

983 Gouin, P., 1979. Earthquake history of Ethiopia and the Horn of Africa. IDRC, Ottawa, ON,
984 CA.

985 Greenfield, T., Keir, D., Kendall, J. M. and Ayele, A., 2019a. Low-frequency earthquakes
986 beneath Tullu Moye volcano, Ethiopia, reveal fluid pulses from shallow magma
987 chamber. Earth and Planetary Science Letters, 526: 115782.

988 Greenfield, T., Keir, D., Kendall, J. M. and Ayele, A., 2019b. Seismicity of the Bora-Tullu Moye
989 Volcanic Field, 2016–2017. Geochemistry, Geophysics, Geosystems, 20(2): 548-570.

990 Harangi, S., Molnár, K., Schmitt, A. K., Dunkl, I., Seghedi, I., Novothny, Á., Molnár, M., Kiss,
991 B., Ntaflos, T., Mason, P.R. and Lukács, R., 2020. Fingerprinting the Late Pleistocene
992 tephras of Ciomadul volcano, eastern–central Europe. Journal of Quaternary Science,
993 35(1-2): 232-244.

994 Heiken, G. and McCoy Jr, F., 1984. Caldera development during the Minoan eruption, Thira,
995 Cyclades, Greece. Journal of Geophysical Research: Solid Earth, 89(B10): 8441-8462.

996 Hildreth, W. and Mahood, G. A., 1986. Ring-fracture eruption of the Bishop Tuff. Geological
997 Society of America Bulletin, 97(4): 396-403.

998 Houghton, B. F. and Wilson, C. J. N., 1989. A vesicularity index for pyroclastic deposits.
999 Bulletin of volcanology, 51(6): 451-462.

1000 Hutchison, W., Fusillo, R., Pyle, D. M., Mather, T. A., Blundy, J. D., Biggs, J., Yirgu, G., Cohen,
1001 B.E., Brooker, R.A., Barfod, D.N. and Calvert, A. T., 2016a. A pulse of mid-Pleistocene
1002 rift volcanism in Ethiopia at the dawn of modern humans. Nature Communications,
1003 7(1): 1-12.

1004 Hutchison, W., Pyle, D. M., Mather, T. A., Yirgu, G., Biggs, J., Cohen, B. E., Barfod, D.N. and
1005 Lewi, E., 2016b. The eruptive history and magmatic evolution of Aluto volcano: new
1006 insights into silicic peralkaline volcanism in the Ethiopian rift. Journal of Volcanology
1007 and Geothermal Research, 328: 9-33.

1008 Hutchison, W., Biggs, J., Mather, T. A., Pyle, D. M., Lewi, E., Yirgu, G., Caliro, S., Chiodini, G.,
1009 Clor, L.E. and Fischer, T. P., 2016c. Causes of unrest at silicic calderas in the East
1010 African Rift: New constraints from InSAR and soil-gas chemistry at Aluto volcano,
1011 Ethiopia. Geochemistry, Geophysics, Geosystems, 17(8): 3008-3030.

1012 Jochum, K. P., Stoll, B., Herwig, K., Willbold, M., Hofmann, A. W., Amini, M., Aurburg, S.,
1013 Abouchami, W., Hellebrand E. and Raczek, I., 2006. MPI-DING reference glasses for in
1014 situ microanalysis: New reference values for element concentrations and isotope
1015 ratios. Geochemistry, Geophysics, Geosystems, 7(2).

1016 Jochum, K. P., Weis, U., Stoll, B., Kuzmin, D., Yang, Q., Raczek, I.,Jacobe, D.E, Stracke, A.,
1017 Birbaum, K., Frick, D.A. and Günther, D., 2011. Determination of reference values for
1018 NIST SRM 610–617 glasses following ISO guidelines. Geostandards and Geoanalytical
1019 Research, 35(4): 397-429.

1020 Jordan, N. J., Rotolo, S. G., Williams, R., Speranza, F., McIntosh, W. C., Branney, M. J. and
1021 Scaillet, S., 2018. Explosive eruptive history of Pantelleria, Italy: Repeated caldera
1022 collapse and ignimbrite emplacement at a peralkaline volcano. Journal of Volcanology
1023 and Geothermal Research, 349: 47-73.

1024 Kazmin, V. and Berhe, S. M., 1978. Geology and development of the Nazret area. Northern
1025 Ethiopian Rift sheet NC37–15, Memoir, 3: 26.

1026 Keir, D., Ebinger, C. J., Stuart, G. W., Daly, E. and Ayele, A., 2006. Strain accommodation by
1027 magmatism and faulting as rifting proceeds to breakup: Seismicity of the northern
1028 Ethiopian rift. Journal of Geophysical Research: Solid Earth, 111(B5).

1029 Korme, T., Acocella, V. and Abebe, B., 2004. The role of pre-existing structures in the origin,
1030 propagation and architecture of faults in the Main Ethiopian Rift. Gondwana Research,
1031 7(2): 467-479.

1032 Le Bas, M. J., Maitre, R. L., Streckeisen, A., Zanettin, B. and IUGS Subcommission on the
1033 Systematics of Igneous Rocks, 1986. A chemical classification of volcanic rocks based
1034 on the total alkali-silica diagram. Journal of petrology, 27(3): 745-750.

1035 Legros, F., 2000. Minimum volume of a tephra fallout deposit estimated from a single
1036 isopach. Journal of Volcanology and Geothermal Research, 96(1-2): 25-32.

1037 Le Turdu, C., Tiercelin, J. J., Gibert, E., Travi, Y., Lezzar, K. E., Richert, J. P., Massault, M.,
1038 Gesse, F., Bonnefille, R., Decobert, M. and Gensous, B., 1999. The Ziway–Shala lake
1039 basin system, Main Ethiopian Rift: influence of volcanism, tectonics, and climatic
1040 forcing on basin formation and sedimentation. Palaeogeography, Palaeoclimatology,
1041 Palaeoecology, 150(3-4): 135-177.

1042 Lipman, P. W., 1984. The roots of ash flow calderas in western North America: windows into
1043 the tops of granitic batholiths. Journal of Geophysical Research: Solid Earth, 89(B10):
1044 8801-8841.

1045 Loughlin, S. C., Sparks, R. S. J., Sparks, S., Brown, S. K., Jenkins, S. F. and Vye-Brown, C., 2015.
1046 Global volcanic hazards and risk. Cambridge University Press.

1047 Lowe, D. J., 2011. Tephrochronology and its application: a review. Quaternary
1048 Geochronology, 6(2): 107-153.

1049 Macdonald, R., 1974. Nomenclature and petrochemistry of the peralkaline oversaturated
1050 extrusive rocks. Bulletin volcanologique, 38(2): 498-516.

1051 Mamo, T., 2002. Surface hydrothermal alteration in the Tullu Moye area, Lakes district rift,
1052 Ethiopia. Geological Survey of Ethiopia, Addis Ababa, 7 pp.

1053 Martin-Jones, C. M., Lane, C. S., Pearce, N. J., Smith, V. C., Lamb, H. F., Schaebitz, F.,
1054 Viehberg, F., Brown, M.C., Frank, U. and Asrat, A., 2017. Recurrent explosive eruptions
1055 from a high-risk Main Ethiopian Rift volcano throughout the Holocene. Geology,
1056 45(12): 1127-1130.

1057 McNamara, K., Cashman, K. V., Rust, A. C., Fontijn, K., Chalié, F., Tomlinson, E. L. and Yirgu,
1058 G., 2018. Using lake sediment cores to improve records of volcanism at Aluto volcano
1059 in the Main Ethiopian Rift. Geochemistry, Geophysics, Geosystems, 19(9): 3164-3188.

1060 Mulugeta, B. D., Fujimitsu, Y., Nishijima, J. and Saibi, H., 2021. Interpretation of gravity data
1061 to delineate the subsurface structures and reservoir geometry of the Aluto–Langano
1062 geothermal field, Ethiopia. Geothermics, 94: 102093.

1063 Niespolo, E. M., Rutte, D., Deino, A. L. and Renne, P. R., 2017. Intercalibration and age of the
1064 Alder Creek sanidine 40Ar/39Ar standard. Quaternary Geochronology, 39: 205-213.

1065 Peccerillo, A., Barberio, M. R., Yirgu, G., Ayalew, D., Barbieri and Wu, T. W., 2003.
1066 Relationships between mafic and peralkaline silicic magmatism in continental rift
1067 settings: a petrological, geochemical and isotopic study of the Gedemsa volcano,
1068 central Ethiopian rift. Journal of Petrology, 44(11): 2003-2032.

1069 Polacci, M., Pioli, L. and Rosi, M., 2003. The Plinian phase of the Campanian Ignimbrite
1070 eruption (Phlegrean Fields, Italy): evidence from density measurements and textural
1071 characterization of pumice. Bulletin of Volcanology, 65(6): 418-432.

1072 Pyle, D. M., 1989. The thickness, volume and grainsize of tephra fall deposits. Bulletin of
1073 Volcanology, 51(1): 1-15.

1074 Pyle, D. M., 2015. Sizes of volcanic eruptions. In The encyclopedia of volcanoes (pp. 257-
1075 264). Academic Press.

1076 Rapprich, V., Žáček, V., Verner, K., Erban, V., Goslar, T., Bekele, Y., Legesa, F., Hroch, T. and
1077 Hejtmánková, P., 2016. Wendo Koshe Pumice: The latest Holocene silicic explosive
1078 eruption product of the Corbetti volcanic system (southern Ethiopia). Journal of
1079 Volcanology and Geothermal Research, 310: 159-171.

1080 Reimer, P. J., Austin, W. E., Bard, E., Bayliss, A., Blackwell, P. G., Ramsey, C. B., Butzin, M.,
1081 Cheng, H., Edwards, R.L., Friedrich, M. and Talamo, S., 2020. The IntCal20 Northern
1082 Hemisphere radiocarbon age calibration curve (0–55 cal kBP). Radiocarbon, 62(4):
1083 725-757.

Renne, P. R., Balco, G., Ludwig, K. R., Mundil, R. and Min, K., 2011. Response to the comment by WH Schwarz et al. on "Joint determination of 40K decay constants and 40Ar∗/40K for the Fish Canyon sanidine standard, and improved accuracy for 40Ar/39Ar geochronology" by PR Renne et al.(2010). Geochimica et Cosmochimica Acta, 75(17): 5097-5100.

Roduit, N., 2019. Image analysis toolbox for measuring and quantifying components of high-definition images, JMicroVision: Version 1.3.1. https://jmicrovision.github.io (accessed 10 August 2020).

Rooney, T., Furman, T., Bastow, I., Ayalew, D. and Yirgu, G., 2007. Lithospheric modification during crustal extension in the Main Ethiopian Rift. Journal of Geophysical Research: Solid Earth, 112(B10).

Schneider, C.A., Rasband, W.S. and Eliceiri, K. W., 2012. NIH Image to ImageJ: 25 years of image analysis. Nature methods, 9(7): 671-675.

Seggiaro, R. E., Guzmán, S. R. and Martí, J., 2019. Dynamics of caldera collapse during the Coranzulí eruption (6.6 Ma)(Central Andes, Argentina). Journal of Volcanology and Geothermal Research, 374: 1-12.

Siegburg, M., Gernon, T. M., Bull, J. M., Keir, D., Barfod, D. N., Taylor, R. N., Abebe, B. and Ayele, A., 2018. Geological evolution of the Boset-Bericha volcanic complex, Main Ethiopian Rift: 40Ar/39Ar evidence for episodic Pleistocene to Holocene volcanism. Journal of Volcanology and Geothermal Research, 351: 115-133.

Smith, V. C., Pearce, N. J., Matthews, N. E., Westgate, J. A., Petraglia, M. D., Haslam, M., Lane, C.S., Korisettar, R. and Pal, J. N., 2011. Geochemical fingerprinting of the

1106 widespread Toba tephra using biotite compositions. Quaternary International, 246(1-
1107 2): 97-104.

1108 Spence, R. J. S., Kelman, I., Baxter, P. J., Zuccaro, G. and Petrazzuoli, S., 2005. Residential
1109 building and occupant vulnerability to tephra fall. Natural Hazards and Earth System
1110 Sciences, 5(4): 477-494.

1111 Teklemariam, M., Battaglia, S., Gianelli, G. and Ruggieri, G., 1996. Hydrothermal alteration in
1112 the Aluto-Langano geothermal field, Ethiopia. Geothermics, 25(6): 679-702.

1113 Tierz, P., Clarke, B., Calder, E. S., Dessalegn, F., Lewi, E., Yirgu, G., Fontijn, K., Crummy, J.M.,
1114 Bekele, Y. and Loughlin, S. C., 2020. Event trees and epistemic uncertainty in long-term
1115 volcanic hazard assessment of rift volcanoes: The example of Aluto (Central Ethiopia).
1116 Geochemistry, Geophysics, Geosystems, 21(10).

1117 United Nations Development Programme (UNDP), 1973. Geology, geochemistry and
1118 hydrology of hot springs of the East African Rift system within Ethiopia. In
1119 Investigation of geothermal resources for power development (Tech. Rep. DP/SF/UN
1120 116, 275 pp.). New York, NY: United Nations.

1121 Varet, J. and Birba, E. Tullu Moye Geothermal Project (Oromia, Ethiopia). In proceedings, 7th
1122 African Rift Geothermal Conference, Kigali, Rwanda 31st October – 2nd November
1123 2018, 15 pp.

1124 Walker, G. P., 1985. Origin of coarse lithic breccias near ignimbrite source vents. Journal of
1125 Volcanology and Geothermal Research, 25(1-2): 157-171.

Wilson, TM, Stewart, C., Sword-Daniels, V., Leonard, GS, Johnston, DM, Cole, JW, Wardman, J., Wilson, G. and Barnard, ST., 2012. Volcanic ash impacts on critical infrastructure. Physics and Chemistry of the Earth, Parts A / B / C, 45: 5-23.

WoldeGabriel, G., Aronson, J. L. and Walter, R. C., 1990. Geology, geochronology, and rift basin development in the central sector of the Main Ethiopia Rift. Geological Society of America Bulletin, 102(4): 439-458.

**Figures**

**Figure 1**: Overview map of the MER and its main volcanic and tectonic features. The location of the BBTM volcanic system is indicated by a dashed rectangle (for a more detailed view, see Fig.2a). Along-rift volcanoes that are considered to be active, with eruptions in the Holocene, are indicated by a red triangle. BJVF: Butajira Volcanic Field; DZVF: Debre Zeyt Volcanic Field, are mainly basaltic lava and scoria cones located at the MER western margin. MER faults after Agostini et al. (2011). Inset shows location of the main map (solid rectangle). The Kenyan rift (KR) is connected to the MER by a broadly rifted zone with little to no surface expression of magmatism. The MER progresses northwards in the Afar Depression forming a triple junction with the Gulf of Aden (GA) and Red Sea (RS) rifts.

**Figure 2**: (A) Map of Bora-Baricha-Tullu Moye volcanic complex showing the distribution of different volcanic centres, visited outcrops (the most important of which are labelled with three digits referring to their MER outcrops name; SM-3) and shallow drill well sites (see Fig. 2b; after Ayele et al. 2002). Some outcrops indicated on this figure are the same as those in Fontijn et al. (2018). The Werdi vent (spelled also Werdia) is locally also known as Dima. The extent of the A-A' profile (Fig. 2b) is indicated by two crosss. (B) West-East (A-A') cross

section showing the sub-surface stratigraphy of BBTM from shallow drill-cores (data from Ayele et al. 2002). The elevation scale on the y axis represents the well stratigraphy; topography is two times vertically exaggerated.

**Figure 3**: Tephrostratigraphic framework of the BBTM volcanic complex. (A) Baricha, Meki and Suke. (B) Bora, Oda, Werdi and Tullu Moye. Correlations between the different sections are based on stratigraphic position, physical characteristics, petrography and glass chemical composition of the deposits. The relative geographic location in the volcanic system and the scale of the stratigraphic sections are indicated on this figure and can be seen in Fig. 2. The symbols used on geochemical plots of each BBTM unit (Figs. 6-8) are shown for cross-reference.

**Figure 4**: Field photographs of some of the BBTM pyroclastic deposits. The representative pictures show type sections for Suke (A), Meki (B), Baricha (C), Bora (D), Werdi (E), Oda (F) and Tullu Moye (G) deposits. The symbols are cross referenced to Figure 2 (stratigraphy) and Figures 6-8 (geochemistry).

**Figure 5**: Componentry and petrography of representative BBTM deposits of (A) Meki, (B) Bora, (C) Werdi, (D) Baricha, (E) Oda and (F) Tullu Moye. For each sample, representative photos illustrating the componentry (left) and petrography (right) are shown, with quantitative results presented on a bar and pie chart respectively. The photos are taken using a stereo zoom and optical petrographic microscope in plane polarised light.

**Figure 6**: BBTM silicic tephra classification based on major element (wt%) glass composition following (A) Le Bas et al. (1986) and (B) Macdonald (1974). The comparative glass chemistry data for Aluto, Corbetti and Gedemsa volcanoes (dashed lines) are from Fontijn et al. (2018), Martin-Jones et al. (2017) and McNamara et al. (2018).

**Figure 7**: Bivariate major element (wt%) plots of the BBTM silicic tephra glass compositions. The dashed lines on the diagrams indicate the range of compositions of Aluto, Corbetti and Gedemsa tephra from Fontijn et al. (2018), Martin-Jones et al. (2017) and McNamara et al. (2018). Symbols and colours are the same as in Figure 6.

**Figure 8**: BBTM tephra trace element (ppm) bivariate and ratio plots. The red dashed line shows the compositional range of Aluto tephra (from McNamara et al. 2018). Symbols and colours are the same as in Figure 6.

**Figure 9**: Isopach maps (contours in m) for the four major fall deposits from Baricha and Bora, each identified in at least 4 different locations. The minimum (bulk deposit) volume and unit names are indicated on the figures. Volumes are calculated using the Pyle (1989) method for Ba-P4 and Ba-P5, and the Legros (2000) method for Ba-P7 and Bo-P2. Dashed isopach lines are used instead of solid lines where there is great uncertainty in the shape of the contour due to data lack of exposure. The source volcanic centre is indicated by a red triangle and data points by annotated circles.

**Tables**

**Table 1:** Compilation of new and existing BBTM age constraints. The $^{40}Ar/^{39}Ar$ ages are quoted with 2σ standard error. Radiocarbon dates were calibrated in OxCal v.4.4 (Bronk Ramsey 2009) using the IntCal20 calibration curve (Reimer et al. 2020).

**Table 2**: Synoptic overview of all BBTM pyroclastic deposits that were identified in multiple outcrops, with a description of their field appearance and laboratory-based observations that have helped establishing correlations between sections (Fig. 3). The major deposits are described in more detail in the text. Mineral abbreviations: alkali feldspar (Kfs), aenigmatite

(Ang), feldspar (Fs), pyroxene (Px), orthopyroxene (Opx), clinopyroxene (Cpx), amphibole (Amp). Th: thickness.

**Table 3**: Glass major (wt%) and trace (ppm) element composition of BBTM tephra units. Presented data are average compositions (1 sigma standard deviation in brackets) of one representative sample for each unit. The full data set is provided in supplementary material (SM-2 and SM-5). The analysed number of spots per sample for major (n) and trace (N) elements are indicated.

**Supplementary Information**

**Supplementary material 1 (SM-1)**: SEM-BSE images and EDS spectra on selected points on two BBTM representative samples (MER201H and MER201A).

- **Figure SM-1.1**: (A) BSE image of pumice sample MER201H. (B & C) Glass semi-quantitative EDS spectra for sample spots indicated on the BSE image.
- **Figure SM-1.2**: (A) BSE image of pumice sample MER201A collected from Baricha deposit Ba-P3. (B-D) Semi-quantitative EDS spectra for sample spots indicated on the BSE image of (B) an ilmenite inclusion, (C) a glass rim and (D) an alkali feldspar.

**Supplementary material 2 (SM-2)**: BBTM glass major element dataset analysed by EPMA.

**Supplementary material 3 (SM-3)**: Outcrop locations and names.

**Supplementary material 4 (SM-4)**: BBTM tephra componentry and petrography dataset.

**Supplementary material 5 (SM-5)**: BBTM glass trace element dataset analysed by LA-ICP-MS.

**Supplementary material 6 (SM-6)**: Tephra volume and magnitude estimates of major BBTM explosive eruptions.

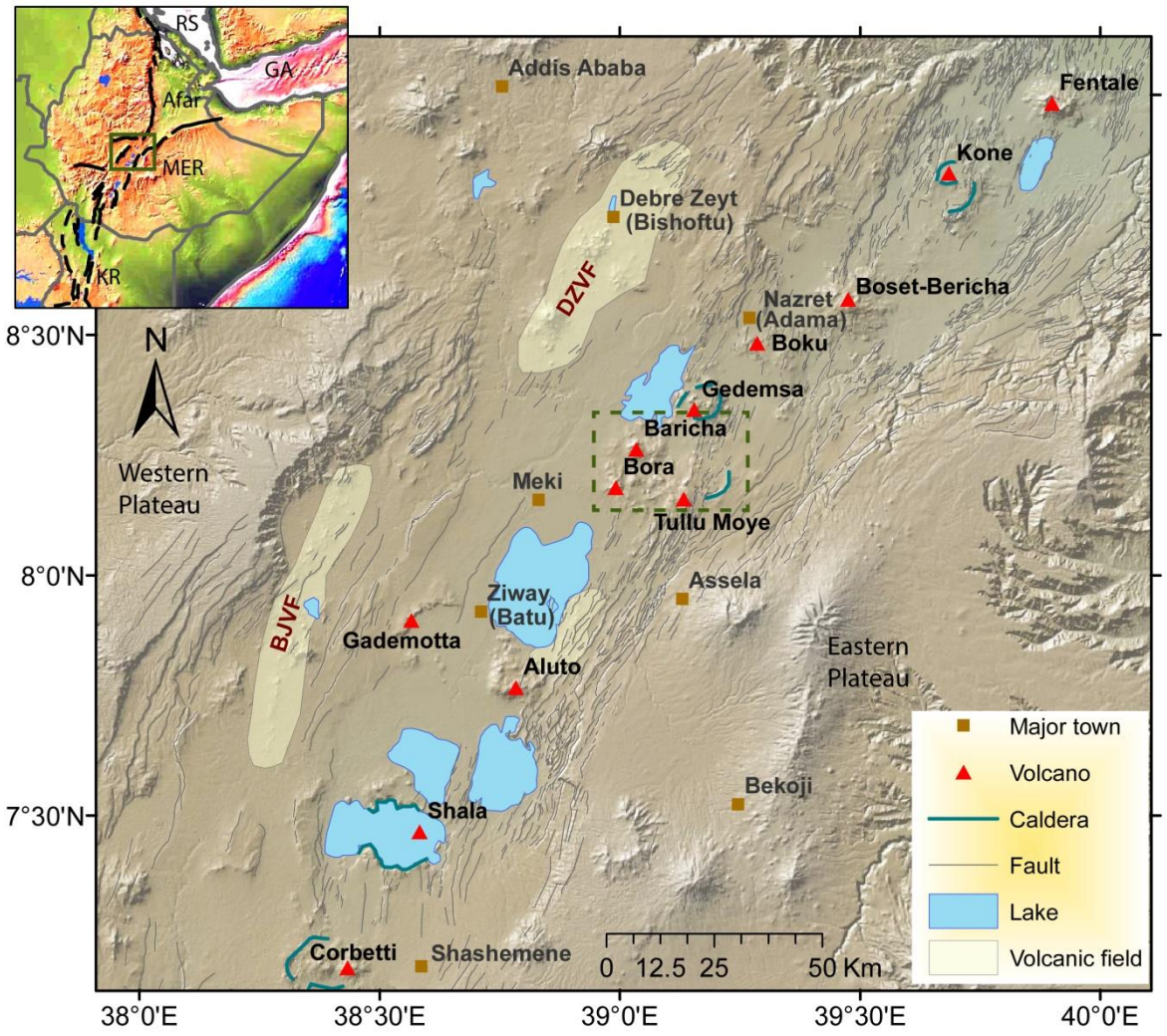
RS
GA
Afar
MER
KR
Addis Ababa
Fentale
Kone
Debre Zeyt
(Bishoftu)
DZVF
Nazret
(Adama)
Boset-Bericha
Boku
Gedemsa
Baricha
Bora
Tullu Moye
Meki
Western
Plateau
Assela
Ziway
(Batu)
BJVF
Gademotta
Aluto
Eastern
Plateau
Bekoji
Shala
Corbetti
Shashemene
Major town
Volcano
Caldera
Fault
Lake
Volcanic field
0 12.5 25 50 Km
N
8°30'N
8°0'N
7°30'N
38°0'E
38°30'E
39°0'E
39°30'E
40°0'E

**Figure 1**

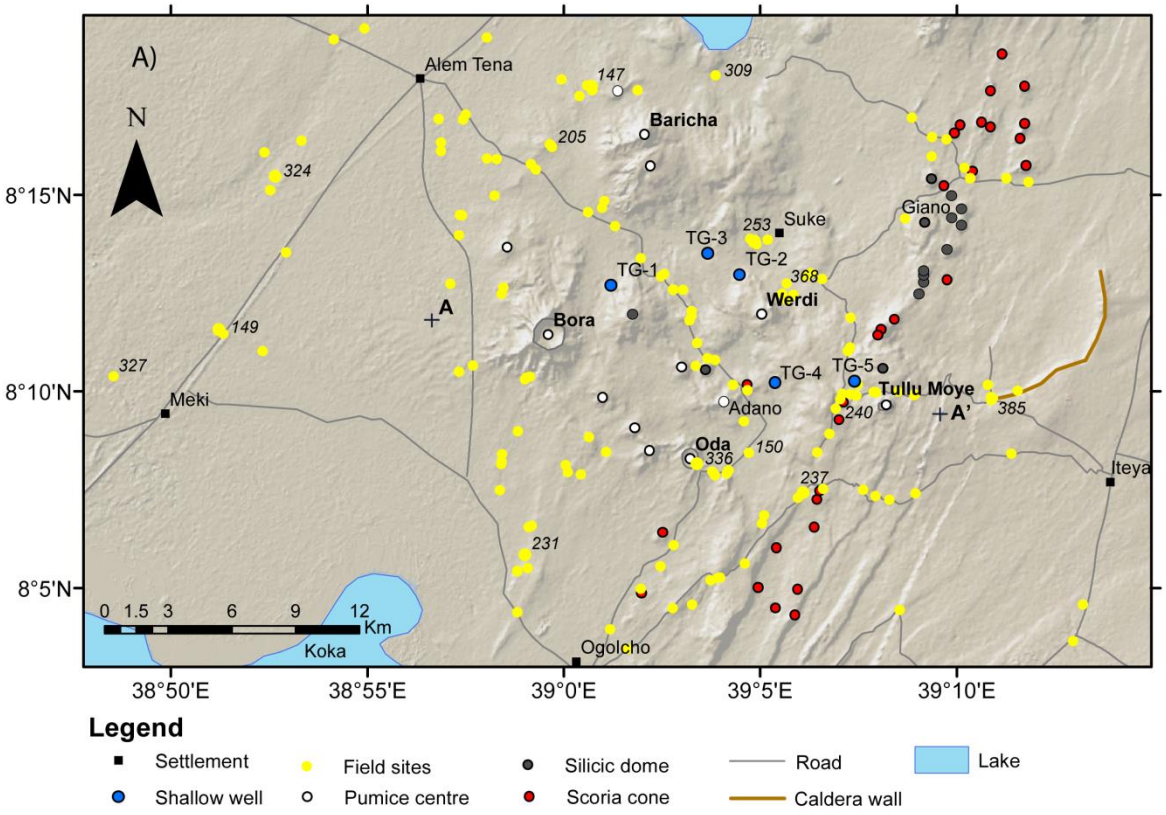
A)
N
Alem Tena
Baricha
Suke
Giano
TG-3
TG-2
TG-1
Werdi
Bora
A
A'
TG-4
TG-5
Tullu Moye
Adano
Oda
Meki
Iteya
Ogolcho
Koka
147
309
205
324
253
368
149
327
240
385
336
150
237
231
0 1.5 3 6 9 12 Km
8°15'N
8°10'N
8°5'N
38°50'E
38°55'E
39°0'E
39°5'E
39°10'E
Legend
Settlement
Field sites
Silicic dome
Road
Lake
Shallow well
Pumice centre
Scoria cone
Caldera wall

**Figure 2a**

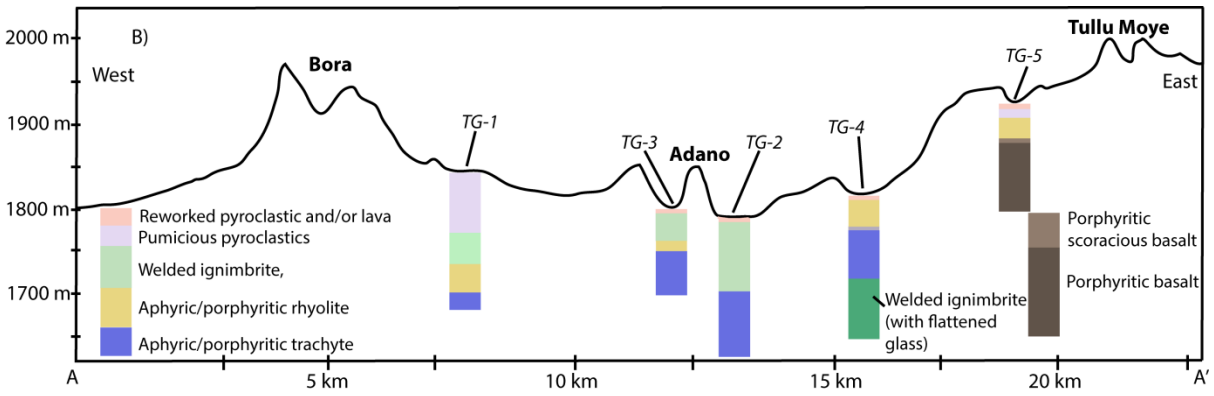
B)
West
East
2000 m
1900 m
1800 m
1700 m
Bora
Adano
Tullu Moye
TG-1
TG-2
TG-3
TG-4
TG-5
Reworked pyroclastic and/or lava
Pumicious pyroclastics
Welded ignimbrite,
Aphyric/porphyritic rhyolite
Aphyric/porphyritic trachyte
Welded ignimbrite (with flattened glass)
Porphyritic scoracious basalt
Porphyritic basalt
A
A'
5 km
10 km
15 km
20 km

**Figure 2b**

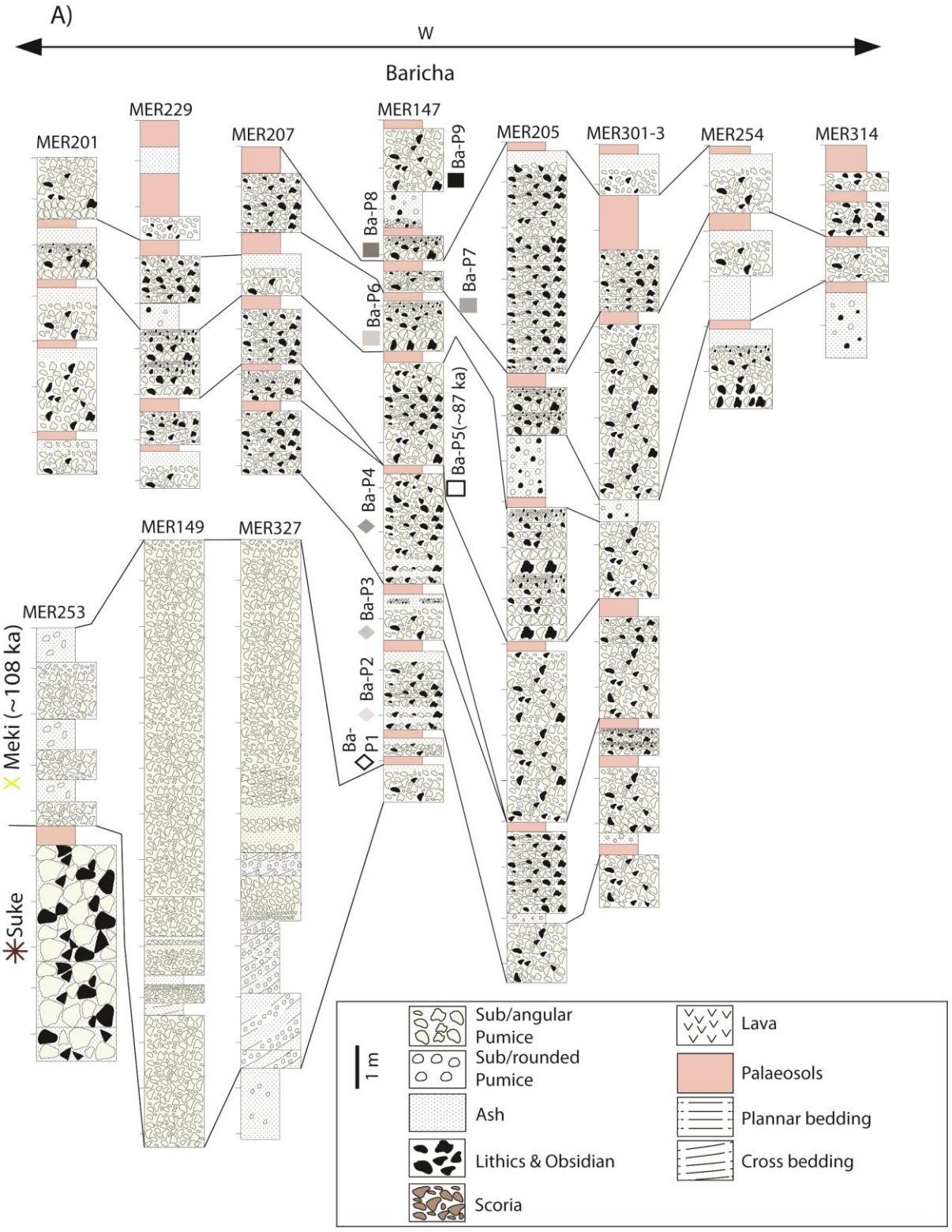
A)
W
Baricha
MER201
MER229
MER207
MER147
MER205
MER301-3
MER254
MER314
MER149
MER327
MER253
Ba-P9
Ba-P8
Ba-P7
Ba-P6
Ba-P5(~87 ka)
Ba-P4
Ba-P3
Ba-P2
Ba-P1
Meki (~108 ka)
Suke
1 m
Sub/angular Pumice
Sub/rounded Pumice
Ash
Lithics & Obsidian
Scoria
Lava
Palaeosols
Plannar bedding
Cross bedding

**Figure 3a**

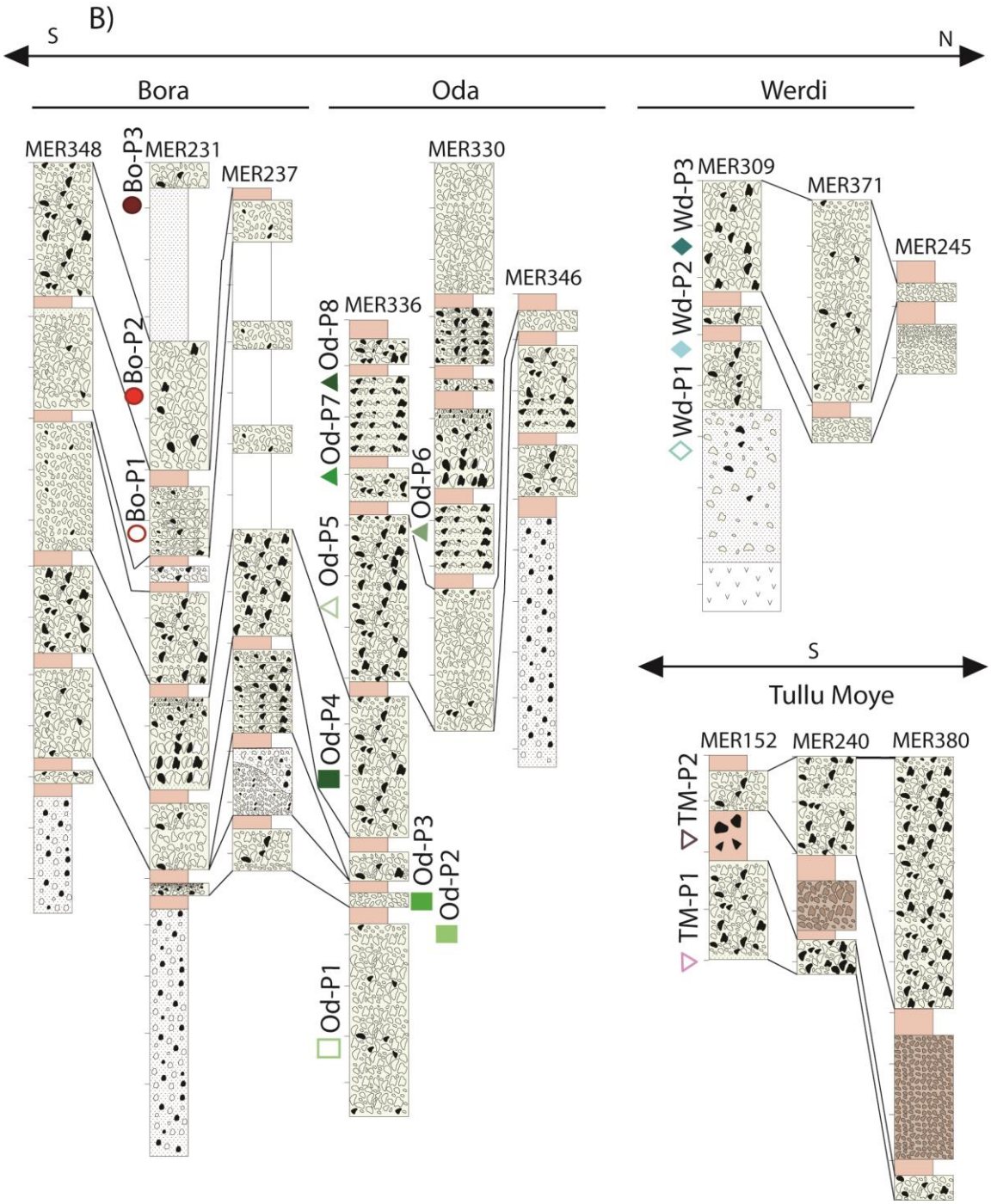
B)
S
N
Bora
Oda
Werdi
MER348
MER231
MER237
MER330
MER346
MER336
MER309
MER371
MER245
Bo-P3
Bo-P2
Bo-P1
Od-P8
Od-P7
Od-P6
Od-P5
Od-P4
Od-P3
Od-P2
Od-P1
Wd-P3
Wd-P2
Wd-P1
S
Tullu Moye
MER152
MER240
MER380
TM-P2
TM-P1

**Figure 3b**

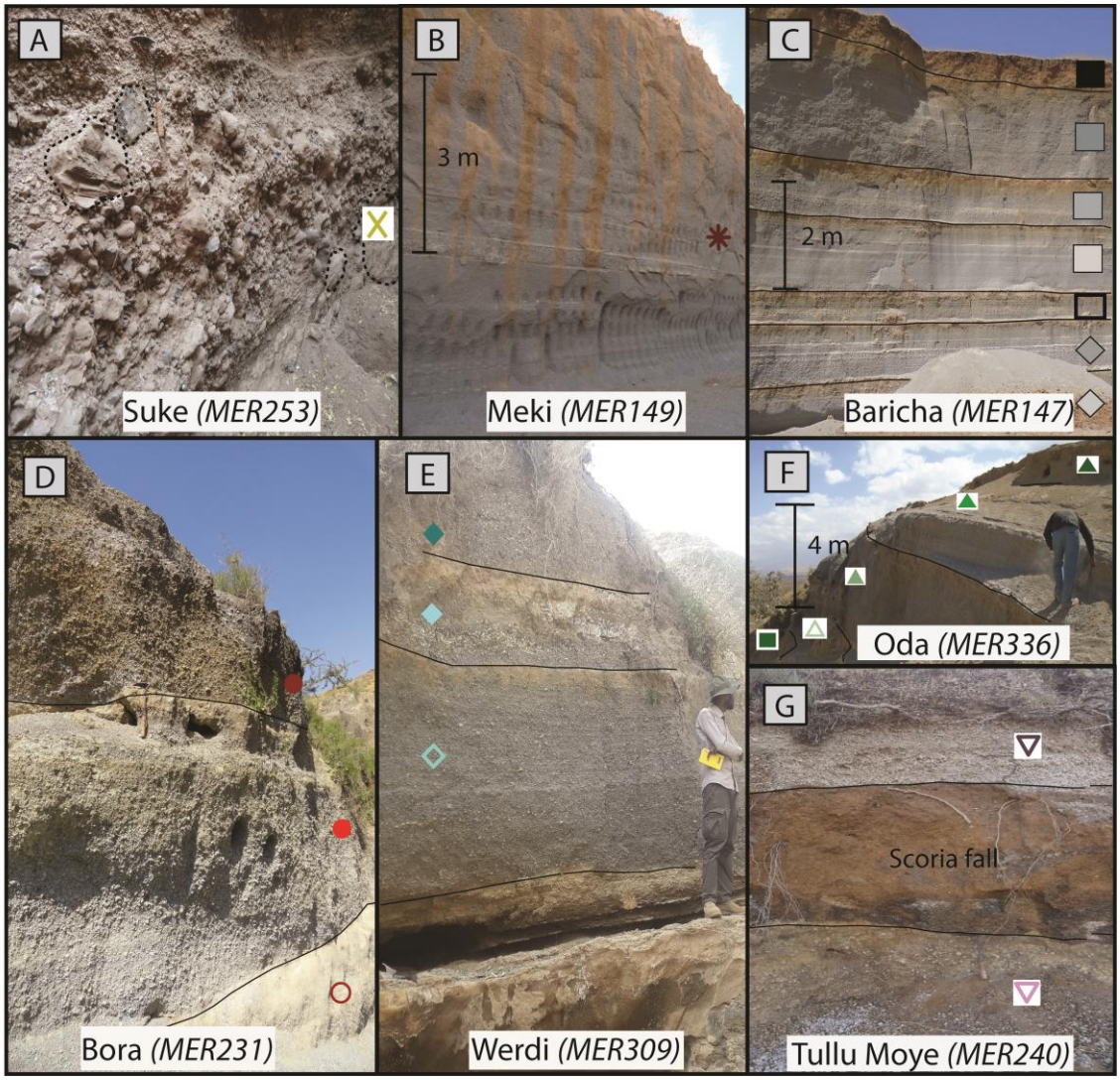
A
Suke (MER253)
B
3 m
Meki (MER149)
C
2 m
Baricha (MER147)
D
Bora (MER231)
E
Werdi (MER309)
F
4 m
Oda (MER336)
G
Scoria fall
Tullu Moye (MER240)

**Figure 4**

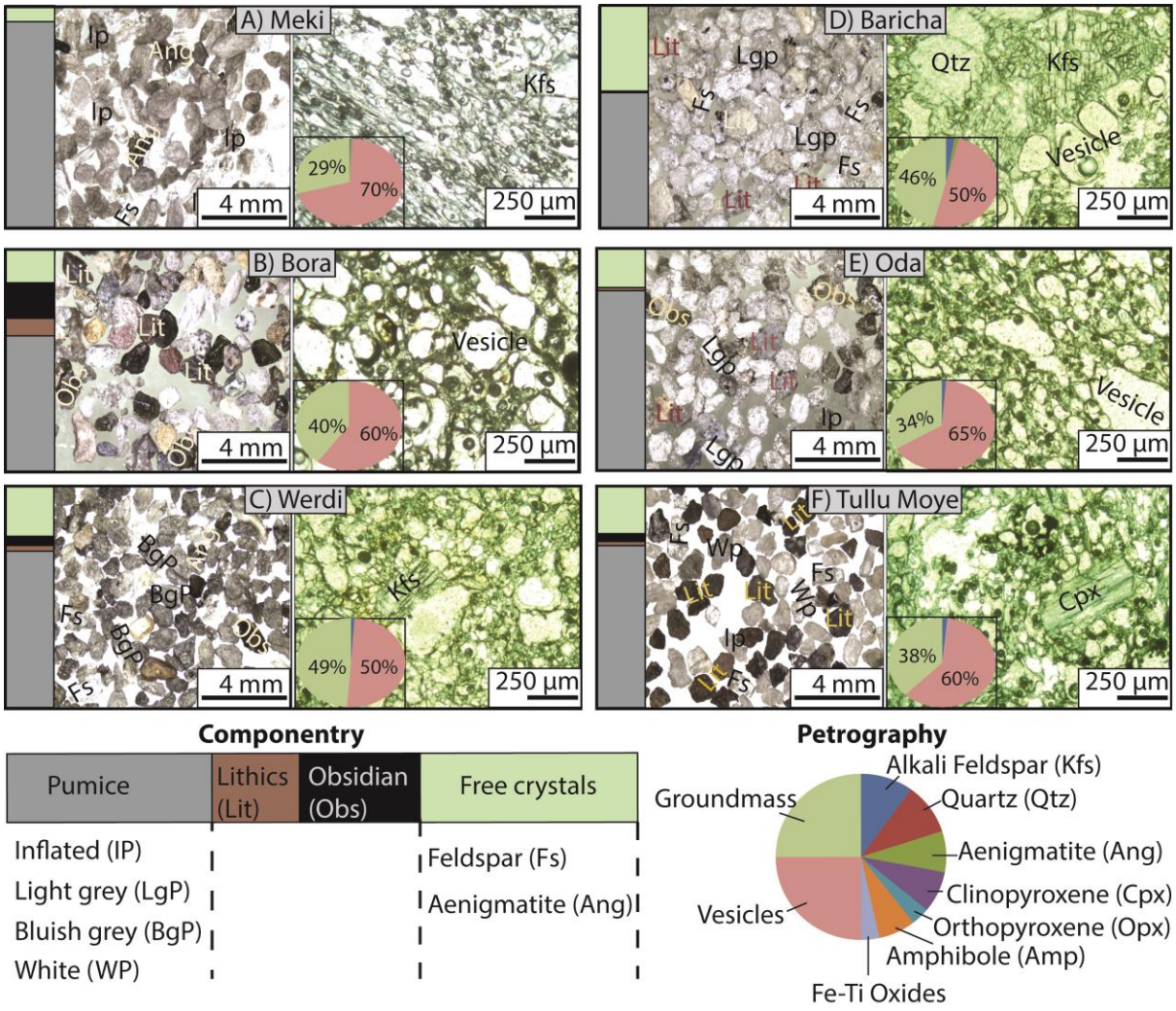
A) Meki
Ip
Ang
Fs
4 mm
Kfs
29%
70%
250 µm
D) Baricha
Lit
Lgp
Fs
Qtz
Kfs
Vesicle
46%
50%
B) Bora
Lit
Obs
Vesicle
40%
60%
E) Oda
Obs
Lgp
Vesicle
34%
65%
C) Werdi
BgP
Fs
Kfs
49%
50%
F) Tullu Moye
Wp
Fs
Cpx
38%
60%
Componentry
Pumice
Lithics (Lit)
Obsidian (Obs)
Free crystals
Inflated (IP)
Light grey (LgP)
Bluish grey (BgP)
White (WP)
Feldspar (Fs)
Aenigmatite (Ang)
Petrography
Groundmass
Alkali Feldspar (Kfs)
Quartz (Qtz)
Aenigmatite (Ang)
Clinopyroxene (Cpx)
Orthopyroxene (Opx)
Amphibole (Amp)
Fe-Ti Oxides
Vesicles

**Figure 5**

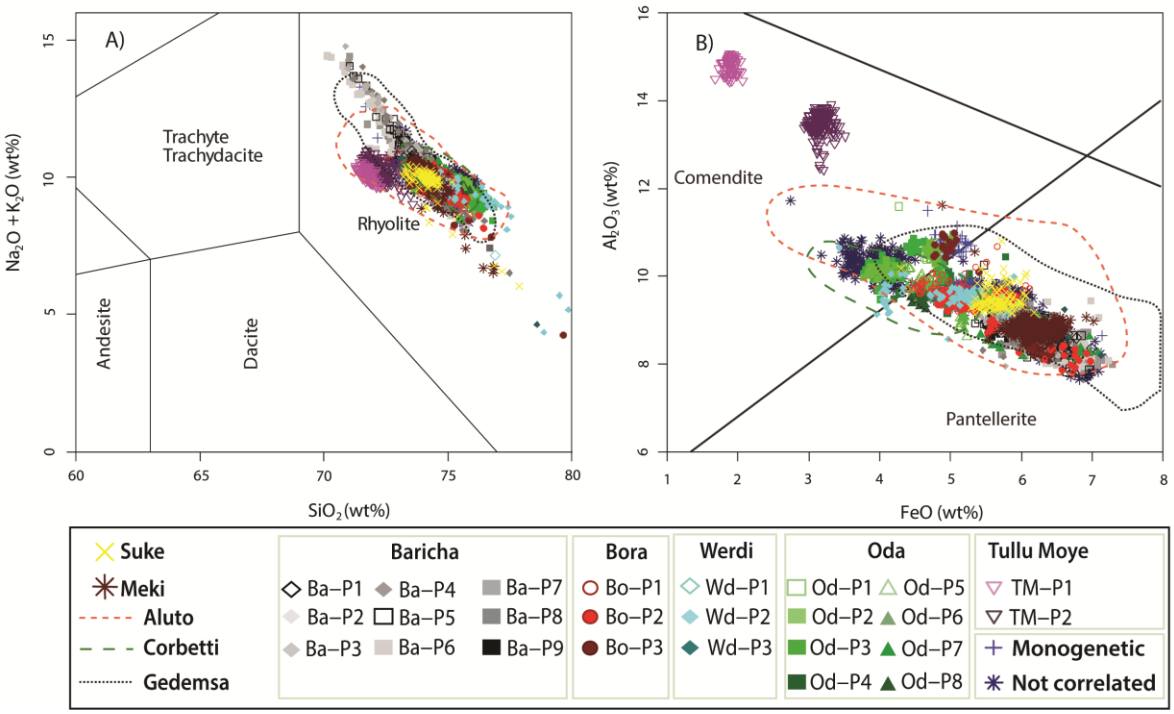
A)
Trachyte
Trachydacite
Rhyolite
Andesite
Dacite
$Na_2O + K_2O$ (wt%)
$SiO_2$ (wt%)
B)
Comendite
Pantellerite
$Al_2O_3$ (wt%)
FeO (wt%)
Suke
Meki
Aluto
Corbetti
Gedemsa
Baricha
Ba–P1 Ba–P4 Ba–P7
Ba–P2 Ba–P5 Ba–P8
Ba–P3 Ba–P6 Ba–P9
Bora
Bo–P1
Bo–P2
Bo–P3
Werdi
Wd–P1
Wd–P2
Wd–P3
Oda
Od–P1 Od–P5
Od–P2 Od–P6
Od–P3 Od–P7
Od–P4 Od–P8
Tullu Moye
TM–P1
TM–P2
Monogenetic
Not correlated

**Figure 6**

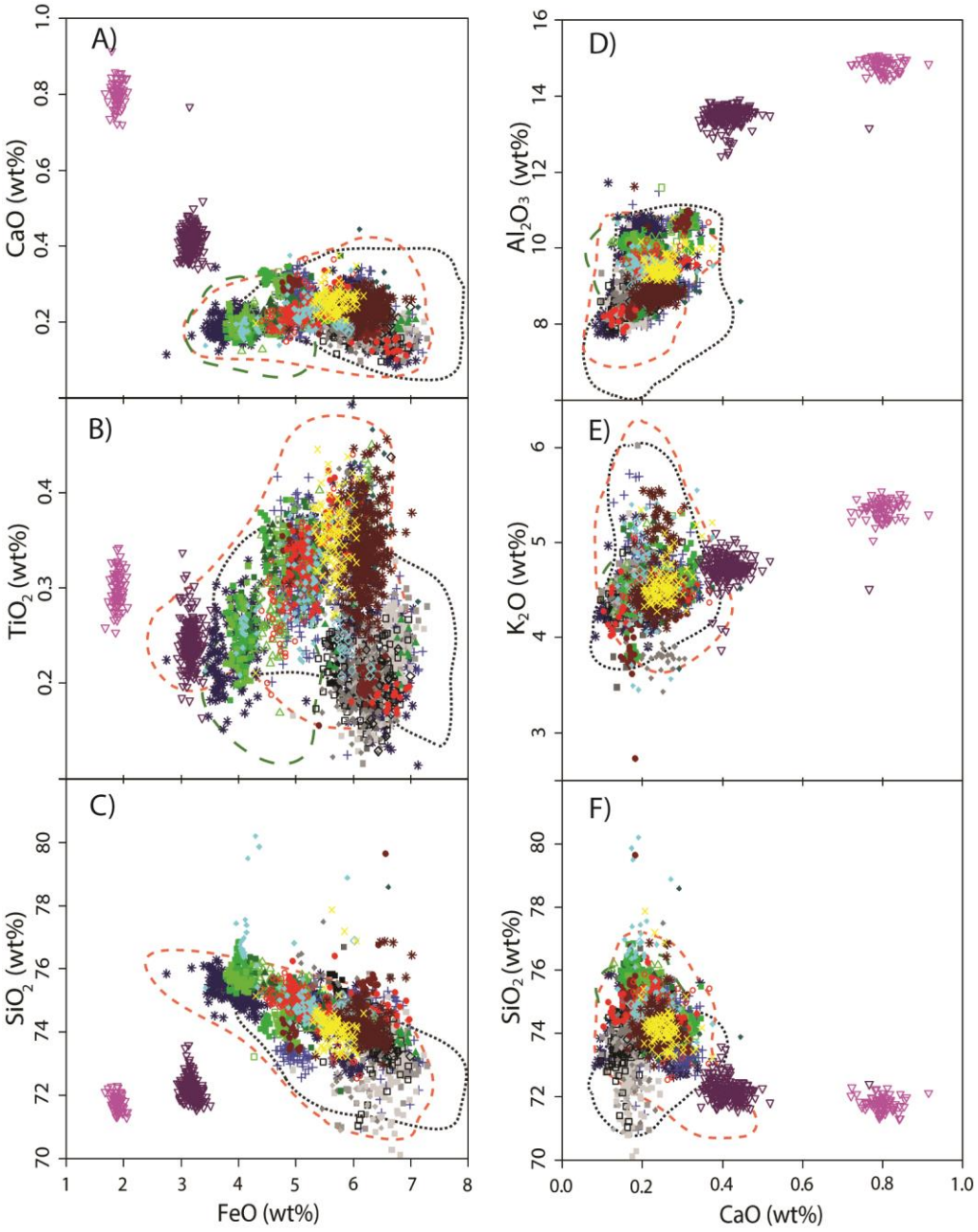


**Figure 7**

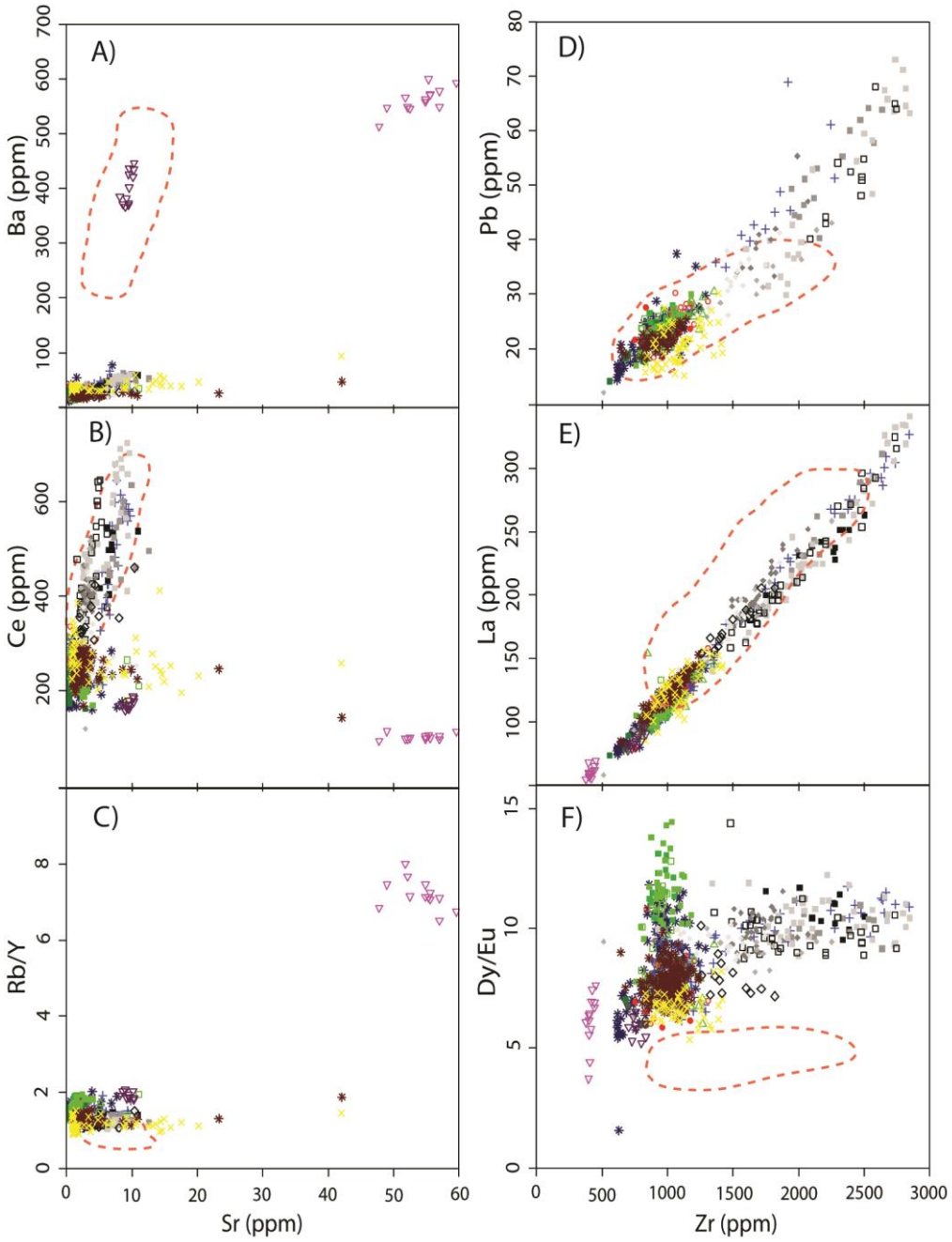


**Figure 8**

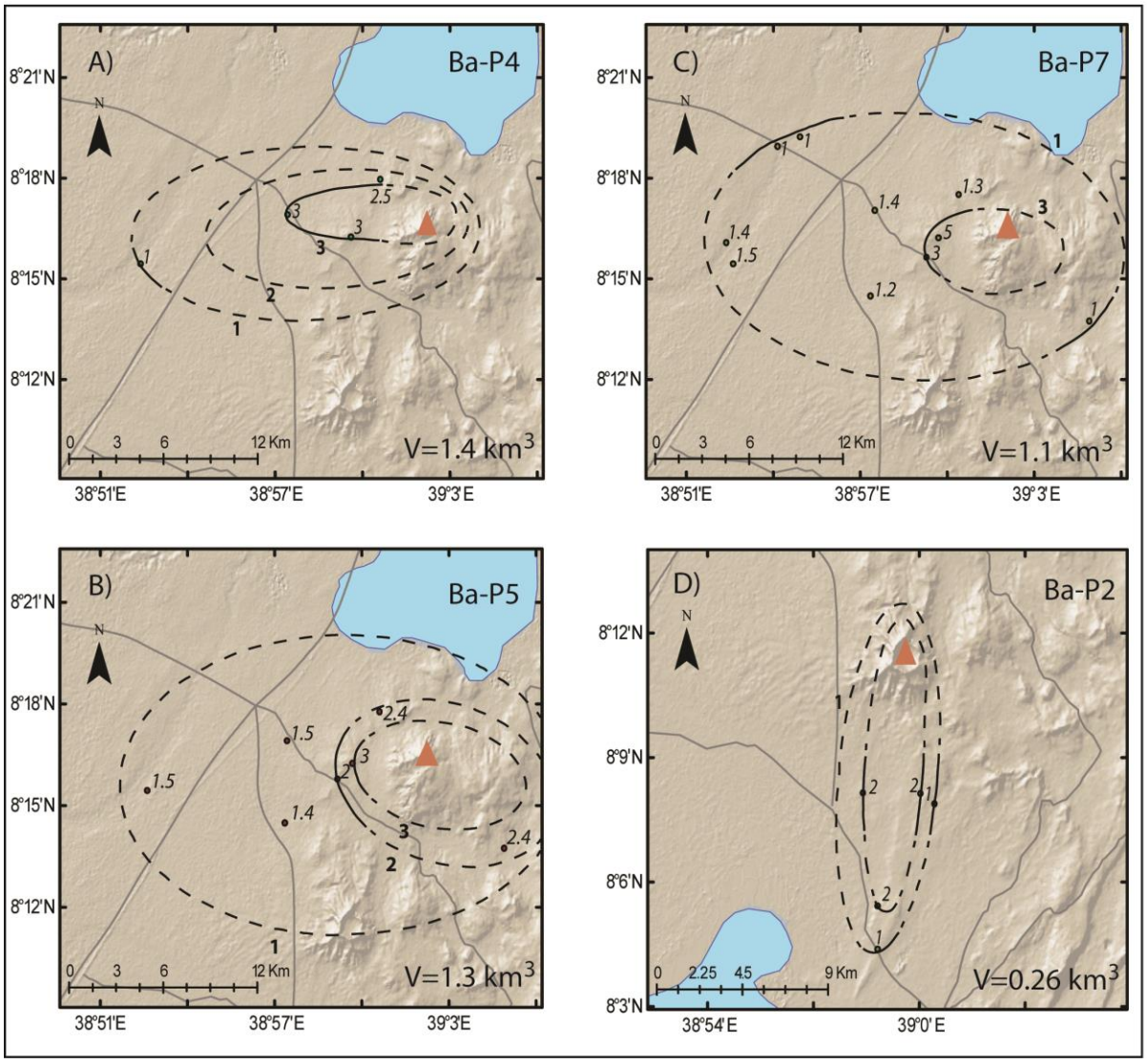
A)
Ba-P4
V=1.4 km3
B)
Ba-P5
V=1.3 km3
C)
Ba-P7
V=1.1 km3
D)
Ba-P2
V=0.26 km3
8°21'N
8°18'N
8°15'N
8°12'N
8°9'N
8°6'N
8°3'N
38°51'E
38°57'E
39°3'E
38°54'E
39°0'E
0 3 6 12 Km
0 2.25 45 9 Km
N

**Figure 9**

**Table 1**

| Volcanic centre | Sample code | Location | | Rock type | Method | Age | Additional note |
|---|---|---|---|---|---|---|---|
| | | Lat | Long | | | | |
| **Unknown** | BT-108 | Unknown | | Obsidian lava | K-Ar | 1.58 ± 0.2 Ma | WoldeGabriel et al. (1990) |
| **BBTM** | MER149A | 8.19 | 38.85 | Tephra | $^{40}Ar/^{39}Ar$ (sanidine) | 107.7 ± 8.8 ka | This study |
| **Baricha** | MER147-2D | 8.29 | 39 | Tephra | $^{40}Ar/^{39}Ar$ (sanidine) | 87 ± 16 ka | This study |
| **Baricha** | MER308 | 8.23 | 39.02 | Tephra | $^{14}C$ (charcoal) | 1190 ± 36 cal yrs BP | This study |

**Table 2**

| Source | Unit | Age | Deposit appearance | Interpretation | Componentry (average of grain size fraction <4 mm unless otherwise indicated) | Petrography | Glass composition | Magnitude |
|---|---|---|---|---|---|---|---|---|
| **BBTM** | **Suke** | | Max. Th: 6 m, very poorly sorted, clast-supported, contains bombs and blocks (max. 1 m) | PDC (ignimbrite/lag breccia) | Microvesicular pumice<br>Lava and glassy obsidian lithics | <1% (Ang) | Pantellerite | Caldera forming |
| **BBTM** | **Meki** | 108±8 ka | Max. Th: >20 m. Top and bottom is massive, well-sorted pumice lapilli breccia with expanded pumice. The middle part is an alternation of poorly and well sorted pumice lapilli breccia beds. The poorly sorted layers have no consistent local thickness, and show mm-scale low-angle cross bedding, and sub-horizontal laminations of poorly sorted and sub-rounded pumice lapilli in fine ash | Sequence of tephra fall (bottom), PDC (middle) and tephra fall (top) | 45-90% microvesicular & ≤40% expanded pumice<br>5-20% free crystals (Fs & Ang)<br>No lithics | 70-75% vesicles<br><1% phenocrysts (Kfs, Ang)<br>Microlite-poor groundmass | Pantellerite | Caldera forming |
| **Baricha** | **Ba-P1** | | Max. Th: 37 cm. Crudely bedded, well sorted and poorly preserved pumice lapilli | Tephra fall | 100% microvesicular pumice | | Pantellerite | |

| | | | | | | | |
|---|---|---|---|---|---|---|---|
| | | breccia | | | | | |
| **Ba-P2** | | Max. Th: 185 cm. Sub-parallel to low angle cross-bedded units of medium ash and crystal-rich lapilli in bottom third. Dm-scale bedded, well sorted lapilli breccia in the middle and upper portions. | PDC; Tephra fall | 60% microvesicular & 2% expanded pumice<br>30% free crystals (Fs/Qtz, Ang/Amp/Px)<br>5% lithics (lava & glassy obsidian) | | Pantellerite | |
| **Ba-P3** | | Max. Th: 3 m. Bottom 5-10 cm is fine indurated ash with accretionary lapilli. The rest is light grey pumice lapilli breccia, well sorted, massive to cm-scale crudely bedded with occasional pumice bombs (~15 cm) | Tephra fall | 80-90% microvesicular pumice<br>≤20% free crystals (Fs, Ang & Px)<br><1% crystal-rich obsidian | 65% vesicles<br>6% phenocrysts (Kfs, Ang, Opx)<br>Glassy groundmass | Pantellerite | 4.1 |
| **Ba-P4** | | Max. Th: 2.5 m. Cm-scale fine pumice lapilli interbedded with yellowish ash beds at the base. Massive well-sorted pumice lapilli breccia with occasional pumice bombs | Tephra fall | 45-75% microvesicular, <5% expanded & ≤1% tube pumice<br>10-35% free crystals (Fs, Ang & Fe-Ti Oxides)<br>≤10% lithics (crystal-rich obsidian, lava & ignimbrite) | 65% vesicles<br><1% phenocrysts (Kfs, Ang)<br>microlite-poor groundmass | Pantellerite | 5.1 |
| **Ba-P5** | 87 ± 16 ka | Max. Th: 2.5 m. Massive to cm-to-dm scale crudely bedded well-sorted pumice lapilli breccia | Tephra fall | 55-75% microvesicular, ≤20% expanded & ≤1% tube pumice<br>5-40% free crystals (Fs, Ang/Px/Amp & Fe-Ti Oxides) | 50-65% vesicles<br><10% phenocrysts (Kfs, Ang, Amp, Opx) | Pantellerite | 5.1 |

| | | | | | | | |
|---|---|---|---|---|---|---|---|
| | | | | ≤5% lithics (crystal-rich obsidian, lava & ignimbrite)<br>≤15% obsidian | Glassy groundmass | | |
| **Ba-P6** | | Max. Th: 4 m. Multiple horizons of normally graded and well-sorted pumice lapilli breccia | Tephra fall | 50-70% microvesicular & <10% expanded pumice<br>30% free crystals (Fs, Ang/Amp & Fe-Ti Oxides)<br>≤2% lithics (crystal-rich obsidian, lava & ignimbrite)<br>≤5% obsidian | 50% vesicles<br><10% phenocrysts (Kfs, Ang, Amp) Glassy groundmass | Pantellerite | 4.8 |
| **Ba-P7** | | Max. Th: 5 m. Dm-scale crudely bedded, overall normally graded, and poorly sorted pumice lapilli breccia with some pumice bombs (10-15 cm) | Tephra fall | 65-85% microvesicular, ≤2% expanded & ≤2% tube pumice<br>5-30% free crystals (Fs, Ang & Fe-Ti Oxides)<br>≤2% lithics (crystal rich obsidian, lava & ignimbrite)<br>≤10% glassy obsidian | 50-55% vesicles<br><1% phenocrysts (Kfs & Ang)<br>Glassy groundmass | Pantellerite | 5 |
| **Ba-P8** | | Max. Th: 80 cm. Poorly preserved, highly altered orange-stained pumice lapilli breccia, well sorted with diffuse normal grading | Tephra fall | 75% microvesicular & <5% expanded pumice<br><20% free crystals (Fs, Ang)<br><5% crystal-rich obsidian lithics | 65% vesicles<br>6% phenocrysts (Kfs & Ang)<br>Glassy groundmass | Pantellerite | |
| **Ba-P9** | 1190 ± 36 cal yr BP | Max. Th: 2.5 m. Cream-coloured, matrix-supported and undulated beds in the | PDC; Tephra fall | 80-100% microvesicular<br><20% free crystals (Fs/Qtz, Ang/Amp/Px) | | Pantellerite | |

| | | | | | | | |
|---|---|---|---|---|---|---|---|
| | | bottom half. Parallel bedded, well-sorted pumice lapilli breccia at the top | | <1% crystal-rich obsidian | | | |
| **Oda** | **Od-P1** | Max. Th: 4 m. Massive to crudely bedded, poorly sorted pumice lapilli breccia with occasional pumice bombs (3.5 cm) | Tephra fall | 100% microvesicular | 50% vesicles<br><3% phenocrysts (Kfs, Ang & Cpx) Glassy groundmass | Pantellerite-Comendite | |
| | **Od-P2** | Max. Th: 30 cm. Poorly sorted coarse pumice lapilli breccia with massive to diffuse normal grading | Tephra fall | 75-80% microvesicula, 1% tube & ≤1% expanded pumice<br>≤10% free crystals (Fs/Qtz & Fe-Ti oxides)<br>≤2% lithics (hydr. altered lava, glassy obsidian & ignimbrite)<br>≤10% obsidian | | Pantellerite-Comendite | |
| | **Od-P3** | Max. Th: 2 m. Massive, poorly sorted coarse to fine pumice lapilli breccia | Tephra fall | 80% microvesicular & 1% tube pumice<br>≤5% free crystals (Fs, Ang/Px/Amp & Fe-Ti oxides)<br>≤3% lithics (hydr. altered lava, glassy obsidian & ignimbrite)<br><10% obsidian | 60% vesicles<br>No phenocrysts Glassy groundmass | Pantellerite-Comendite | |
| | **Od-P4** | Max. Th: 3 m. Cm-scale bedded, each bed set is normally graded pumice lapilli | Tephra fall; PDC | 60-80% microvesicular & ≤1% tube pumice<br>10-20% free crystals (Fs, | 55-65% vesicles<br>≤3% | Pantellerite-Comendite | 4.7 |

| | | | | | | |
|---|---|---|---|---|---|---|
| | breccia underlain by a lithic-rich poorly sorted ash horizon | | Ang, Amp, Px & Fe-Ti oxides)<br>≤25% lithics (hydr. altered lava, glassy obsidian & ignimbrite) | phenocrysts (Kfs, Cpx, Amp, Ang)<br>Glassy to microlite-poor groundmass | | |
| **Od-P5** | Max. Th: 3.5 m. Massive and poorly-sorted pumice lapilli breccia with occasional distinct bigger clasts (3.5 cm) | Tephra fall | 60-70% microvesicular & ≤1% tube pumice<br>5-35% free crystals (Fs/Qtz, Ang/Px/Amp & Fe-Ti oxides)<br>≤3% lithics (hydr. altered lava & glassy obsidian)<br><25% obsidian | | Pantellerite-Comendite | 4.6 |
| **Od-P6** | Max. Th: 90 cm. Main unit is massive poorly sorted pumice lapilli breccia. Its top and bottom are marked by thin ash beds (10-20 cm) | Tephra fall | 95% microvesicular pumice<br>5% lithics (lava & glassy obsidian) | | Pantellerite-Comendite | |
| **Od-P7** | Max. Th: 16 m. Interbedded horizons of coarse ash and rounded fine pumice lapilli, lenticular bedding, well sorted within each bed but deposit is poorly sorted overall | PDC | 70% microvesicular pumice<br><25% free crystals (Fs/Qtz & Fe-Ti oxides)<br>1% lithics (hydr. altered lava, glassy obsidian & ignimbrite)<br><5% obsidian | | Pantellerite-Comendite | |
| **Od-P8** | Max. Th: 1.85 m. Well-sorted coarse pumice lapilli breccia with subtle normal grading | Tephra fall | 90% microvesicular & 1% expanded pumice<br>5% lithics (lava, glassy | | Pantellerite-Comendite | |

| | | | | | | | |
|---|---|---|---|---|---|---|---|
| | | | | obsidian & ignimbrite) | | | |
| **Bora** | **Bo-P1** | Max. Th: 1 m. Dm-scale crudely bedded, well-sorted pumice lapilli breccia; top few centimetres shows interbedding of coarse ash and pumice lapilli | Tephra fall | 80% microvesicular, 5% expanded & 1% tube pumice<br><10% free crystals (Fs/Qtz & Fe-Ti oxides)<br>5% obsidian and lithics (lava, glassy obsidian & ignimbrite) | | Pantellerite-Comendite | |
| | **Bo-P2** | Max. Th: 2.5 m. Cm-scale bedded, well-sorted pumice lapilli breccia with occasional pumice bombs (15 cm) | Tephra fall | 60% microvesicular pumice<br>≤15% free crystals (Fs/Qtz & Fe-Ti oxides)<br><8% (hydr. altered lava, glassy obsidian & ignimbrite)<br>15% obsidian | 60% vesicles<br>No phenocrysts<br>Glassy groundmass | Pantellerite-Comendite | 4.3 |
| | **Bo-P3** | Max. Th: >3 m. Massive, poorly to well-sorted coarse pumice lapilli breccia | Tephra fall | 80% microvesicular, 5% expanded & 3% tube pumice<br>5% free crystals (Fs, Ang, Px & Fe-Ti oxides)<br>≤1% lithics (altered lava, glassy obsidian)<br>5% obsidian | 45% vesicles<br><0.5% phenocrysts (Kfs & Opx)<br>Microlite-poor groundmass | Pantellerite | 4.2 |
| **Werdi** | **Wd-P1** | Max. Th: >15 m. Cm-scale bedded, poorly sorted, coarse ash to medium sized bluish-grey pumice lapilli breccia | Tephra fall | 83% microvesicular pumice<br>5% free crystals (Fs/Qtz, Ang/Px/Amp)<br>10% lithics (hydr. altered | | Pantellerite-Comendite | 4.6 |

| | | | | | | | |
|---|---|---|---|---|---|---|---|
| | | | | lava & crystal-rich obsidian) | | | |
| | **Wd-P2** | Max. Th: 35 cm. Massive, well-sorted, bluish-grey pumice lapilli breccia | Tephra fall | 70% microvesicular pumice<br>20% free crystals (Fs, Ang & Fe-Ti oxides)<br><5% lithics (hydr. altered lava, glassy obsidian & ignimbrite)<br><5% obsidian | 50% vesicles<br>1% phenocrysts (Kfs & Ang)<br>Glassy groundmass | Pantellerite-Comendite | 4.4 |
| | **Wd-P3** | Max. Th: 2.1 m. Massive, poorly sorted, bluish-grey coarse pumice lapilli breccia | Tephra fall | <85% microvesicular pumice<br><10% free crystals (Fs/Qtz, Ang/Px/Amp)<br><10% lithics (hydr. altered lava, glassy obsidian & ignimbrite) | | Pantellerite-Comendite | |
| **Tullu Moye** | **TM-P1** | Max. Th: 3 m. Massive, poorly sorted, white pumice lapilli breccia | Tephra fall | 80-85% microvesicular, ≤2% expanded & <5% tube pumice<br>≤10% free crystals (Fs/Qtz, Px/Amp & Fe-Ti oxides)<br><10% lithics (hydr. altered lava & glassy obsidian) | | Comendite | |
| | **TM-P2** | Max. Th: 2 m. Massive, poorly sorted, white pumice lapilli | Tephra fall | 70-100% microvesicular, ≤1% expanded and ≤1% | 60% vesicles<br>2% | Comendite | 2.8 |

| | | | |
|---|---|---|---|
| | breccia containing occasional pumice bombs (15 cm) | tube pumice<br>≤20% free crystals (Fs, Px/Amp & Fe-Ti oxides)<br><3% (hydr. altered lava & glassy obsidian)<br><5% glassy obsidian | phenocrysts (Kfs, Cpx, Amp & Fe-Ti oxide)<br>Glassy groundmass |

**Table 3**

| Group | **Suke** | **Meki** | | | | | **Baricha** | | | | |
|---|---|---|---|---|---|---|---|---|---|---|---|
| Unit | | | **Ba-P1** | **Ba-P2** | **Ba-P3** | **Ba-P4** | **Ba-P5** | **Ba-P6** | **Ba-P7** | **Ba-P8** | **Ba-P9** |
| Sample (MER) | 253-1D | 149B | 147-4F | 205-2E | 205-2C | 147-2F | 147-2A | 147-1E | 205-1B | 147-1C | 147-1A |
| Major | n=27 | n=30 | n=21 | n=26 | n=26 | n=30 | n=29 | n=24 | n=24 | n=29 | n=12 |
| Trace | N=14 | N=15 | N=14 | N=15 | N=10 | N=9 | N=11 | N=15 | N=14 | | N=11 |
| $SiO_2$ | 73.92(0.6) | 74.08(0.3) | 73.65(0.2) | 73.91(0.6) | 73.36(1.2) | 74.03(0.2) | 74.54(0.3) | 74.01(0.4) | 73.12(1.0) | 73.75(0.3) | 73.97(0.2) |
| $TiO_2$ | 0.36(0.1) | 0.33(0.0) | 0.22(0.1) | 0.22(0.0) | 0.22(0.0) | 0.19(0.0) | 0.23(0.0) | 0.18(0.0) | 0.21(0.0) | 0.20(0.0) | 0.21(0.0) |
| $Al_2O_3$ | 9.83(0.4) | 8.72(0.1) | 8.51(0.2) | 9.04(0.2) | 8.45(0.4) | 8.57(0.1) | 8.94(0.1) | 8.74(0.4) | 8.43(0.1) | 8.45(0.1) | 8.61(0.1) |
| FeO | 5.65(0.3) | 6.10(0.2) | 6.51(0.2) | 5.80(0.1) | 6.12(0.4) | 6.30(0.2) | 5.77(0.2) | 6.08(0.3) | 6.25(0.3) | 6.36(0.2) | 6.21(0.2) |
| MnO | 0.21(0.0) | 0.23(0.0) | 0.28(0.1) | 0.24(0.0) | 0.23(0.0) | 0.27(0.1) | 0.22(0.0) | 0.23(0.0) | 0.24(0.0) | 0.27(0.0) | 0.23(0.0) |
| MgO | 0.01(0.0) | 0.01(0.0) | 0.01(0.0) | 0.02(0.0) | 0.01(0.0) | 0.01(0.0) | 0.01(0.0) | 0.01(0.0) | 0.00(0.0) | 0.01(0.0) | 0.01(0.0) |
| CaO | 0.28(0.0) | 0.23(0.0) | 0.21(0.0) | 0.20(0.0) | 0.17(0.0) | 0.18(0.0) | 0.20(0.0) | 0.17(0.0) | 0.16(0.0) | 0.16(0.0) | 0.17(0.0) |
| $Na_2O$ | 4.97(0.7) | 5.87(0.2) | 6.22(0.2) | 6.0(0.7) | 7.00(1.5) | 6.0(0.2) | 5.62(0.1) | 6.08(0.3) | 7.14(1.2) | 6.34(0.2) | 6.17(0.2) |
| $K_2O$ | 4.74(0.3) | 4.4(0.1) | 4.39(0.1) | 4.55(0.1) | 4.43(0.2) | 4.45(0.1) | 4.47(0.1) | 4.49(0.2) | 4.43(0.1) | 4.45(0.1) | 4.42(0.1) |
| Rb | 118 | 129 | 187 | 151 | 198 | 217 | 200 | 250 | 282 | | 284 |
| Sr | 11 | 2 | 4 | 4 | 3 | 3 | 3 | 3 | 8 | | 7 |
| Y | 100 | 100 | 154 | 119 | 168 | 176 | 167 | 200 | 220 | | 207 |
| Zr | 1105 | 876 | 1443 | 1116 | 1653 | 1597 | 1664 | 2018 | 2240 | | 2219 |
| Nb | 149 | 138 | 225 | 169 | 246 | 266 | 255 | 313 | 318 | | 315 |

| | | | | | | | | | | |
|---|---|---|---|---|---|---|---|---|---|---|
| Cs | 1 | 2 | 2 | 2 | 2 | 3 | 2 | 3 | 4 | 4 |
| Ba | 46 | 19 | 23 | 21 | 26 | 20 | 23 | 24 | 51 | 46 |
| La | 114 | 112 | 170 | 134 | 187 | 188 | 180 | 216 | 255 | 239 |
| Ce | 246 | 225 | 344 | 273 | 383 | 390 | 364 | 452 | 519 | 488 |
| Nd | 107 | 101 | 151 | 119 | 159 | 179 | 157 | 190 | 217 | 195 |
| Sm | 23 | 20 | 32 | 25 | 33 | 34 | 32 | 38 | 42 | 39 |
| Eu | 3 | 3 | 4 | 3 | 3 | 3 | 3 | 3 | 4 | 4 |
| Gd | 19 | 19 | 28 | 21 | 27 | 31 | 29 | 36 | 37 | 36 |
| Dy | 20 | 19 | 31 | 22 | 29 | 34 | 31 | 37 | 40 | 39 |
| Yb | 12 | 11 | 16 | 12 | 17 | 19 | 18 | 22 | 23 | 24 |
| Hf | 25 | 21 | 36 | 26 | 34 | 40 | 38 | 47 | 52 | 53 |
| Ta | 10 | 8 | 15 | 10 | 13 | 16 | 15 | 18 | 20 | 20 |
| Th | 20 | 17 | 27 | 21 | 28 | 31 | 29 | 35 | 42 | 40 |
| U | 4 | 4 | 7 | 5 | 6 | 8 | 7 | 9 | 11 | 10 |

Table 3 continued

| Group | | **Werdi** | | | | | **Oda** | | | | |
|---|---|---|---|---|---|---|---|---|---|---|---|
| Unit | **Wd-P1** | **Wd-P2** | **Wd-P3** | **Od-P1** | **Od-P2** | **Od- P3** | **Od-P4** | **Od-P5** | **Od-P6** | **Od-P7** | **Od-P8** |
| Sample (MER) | 368B n=18 | 155B n=28 | 155A n=23 | 336I n=19 | 336H n=17 | 336G n=28 | 336F n=18 | 336D n=14 | 336C n=18 | 330B n=16 | 336A n=19 |
| $SiO_2$ | 74.79(0.6) | 74.76(0.9) | 74.03(1.1) | 74.18(0.4) | 74.11(0.4) | 74.34(0.3) | 75.11(0.4) | 75.24(0.4) | 74.90(0.4) | 74.27(0.6) | 75.14(0.5) |
| $TiO_2$ | 0.24(0.0) | 0.31(0.0) | 0.37(0.1) | 0.34(0.0) | 0.35(0.0) | 0.35(0.0) | 0.33(0.0) | 0.31(0.0) | 0.34(0.0) | 0.24(0.0) | 0.34(0.0) |
| $Al_2O_3$ | 8.94(0.2) | 9.57(0.1) | 8.82(0.2) | 10.60(0.3) | 10.58(0.2) | 10.49(0.3) | 9.72(0.3) | 9.20(0.3) | 9.30(0.3) | 8.34(0.2) | 9.42(0.1) |
| FeO | 5.93(0.2) | 5.23(0.3) | 6.29(0.3) | 4.71(0.1) | 4.82(0.1) | 4.62(0.2) | 4.96(0.1) | 5.23(0.1) | 5.29(0.1) | 6.35(0.7) | 5.00(0.5) |
| MnO | 0.23(0.0) | 0.20(0.0) | 0.24(0.1) | 0.19(0.0) | 0.19(0.0) | 0.19(0.0) | 0.19(0.0) | 0.21(0.0) | 0.21(0.0) | 0.28(0.0) | 0.21(0.0) |
| MgO | 0.02(0.0) | 0.01(0.0) | 0.01(0.0) | 0.02(0.0) | 0.01(0.0) | 0.01(0.0) | 0.01(0.0) | 0.01(0.0) | 0.01(0.0) | 0.01(0.0) | 0.01(0.0) |
| CaO | 0.2(0.0) | 0.24(0.0) | 0.28(0.1) | 0.29(0.0) | 0.30(0.0) | 0.32(0.0) | 0.24(0.0) | 0.21(0.0) | 0.22(0.0) | 0.21(0.0) | 0.23(0.0) |
| $Na_2O$ | 4.90(0.8) | 5.04(0.9) | 5.53(1.0) | 5.08(0.2) | 5.02(0.2) | 4.99(0.4) | 4.90(0.2) | 5.16(0.1) | 5.24(0.2) | 5.79(0.3) | 5.11(0.2) |

| | | | | | | | | | | | |
|---|---|---|---|---|---|---|---|---|---|---|---|
| $K_2O$ | 4.76(0.3) | 4.61(0.4) | 4.42(0.2) | 4.59(0.2) | 4.60(0.2) | 4.67(0.2) | 4.53(0.2) | 4.44(0.1) | 4.48(0.2) | 4.51(0.1) | 4.52(0.2) |

Table 3 continued

| Group | | **Bora** | | **Tullu Moye** | |
|---|---|---|---|---|---|
| Unit | **Bo-P1** | **Bo-P2** | **Bo-P3** | **TM-P1** | **TM-P2** |
| Sample (MER) | 231D n=28 N= | 231B n=30 N=15 | 230A n=28 | 152A n=24 N=12 | 152B n=24 N=13 |
| $SiO_2$ | 74.08(0.8) | 74.65(0.2) | 75.40(1.0) | 72.06(0.2) | 71.74(0.2) |
| $TiO_2$ | 0.34(0.0) | 0.32(0.0) | 0.20(0.0) | 0.24(0.0) | 0.30(0.0) |
| $Al_2O_3$ | 9.46(0.2) | 9.36(0.1) | 8.43(0.4) | 13.28(0.1) | 14.60(0.1) |
| FeO | 5.43(0.4) | 5.18(0.1) | 6.22(0.2) | 3.17(0.2) | 1.89(0.1) |
| MnO | 0.21(0.1) | 0.19(0.0) | 0.24(0.0) | 0.15(0.0) | 0.07(0.0) |
| MgO | 0.01(0.0) | 0.01(0.0) | 0.01(0.0) | 0.08(0.0) | 0.24(0.0) |
| CaO | 0.24(0.0) | 0.22(0.0) | 0.17(0.0) | 0.41(0.0) | 0.80(0.0) |
| $Na_2O$ | 5.74(0.3) | 5.64(0.1) | 5.37(0.9) | 5.85(0.2) | 4.93(0.2) |
| $K_2O$ | 4.48(0.1) | 4.41(0.1) | 3.94(0.4) | 4.74(0.1) | 5.37(0.1) |
| Rb | 159 | 147 | | 126 | 171 |
| Sr | 1 | 1 | | 9 | 54 |
| Y | 105 | 98 | | 66 | 24 |
| Zr | 984 | 977 | | 766 | 415 |
| Nb | 166 | 150 | | 112 | 66 |
| Cs | 2 | 2 | | 1 | 2 |
| Ba | 28 | 25 | | 401 | 562 |
| La | 120 | 112 | | 85 | 60 |
| Ce | 254 | 235 | | 172 | 103 |
| Nd | 109 | 101 | | 72 | 31 |
| Sm | 21 | 20 | | 13 | 5 |

| | | | | |
|---|---|---|---|---|
| Eu | 3 | 3 | 2 | 1 |
| Gd | 18 | 18 | 12 | 4 |
| Dy | 19 | 18 | 12 | 4 |
| Yb | 11 | 11 | 8 | 3 |
| Hf | 24 | 22 | 18 | 10 |
| Ta | 10 | 9 | 7 | 5 |
| Th | 21 | 20 | 17 | 24 |
| U | 5 | 5 | 4 | 6 |